2004

MICRO ELECTRO-DISCHARGE MACHINING: TECHNIQUES AND PROCEDURES FOR MICRO FABRICATION

Christopher James Morgan
University of Kentucky, cjmorg1@uky.edu

ABSTRACT OF THESIS

MICRO ELECTRO-DISCHARGE MACHINING: TECHNIQUES AND PROCEDURES FOR MICRO FABRICATION

Using a Panasonic MG-72 Micro Electro-Discharge Machine, techniques and procedures are developed to fabricate complex microstructures in conductive materials and engineered ceramics.

KEYWORDS: Micro EDM, Machining, Grinding, WEDG, Micro Mechanical Systems

Christopher James Morgan

9/15/04

MICRO ELECTRO-DISCHARGE MACHINING: TECHNIQUES AND PROCEDURES FOR MICRO FABRICATION

By

Christopher James Morgan

Director of Thesis:
Ryan Vallance

Director of Graduate Studies:
George Huang

RULES FOR THE USE OF THESES

Unpublished theses submitted for the Master's degree and deposited in the University of Kentucky Library are a rule open for inspection, but are to be used only with due regard to the rights of the authors. Bibliographical references may be noted, but quotations or summaries of parts may be published only with the permission of the author, and with the usual scholarly acknowledgements.

Extensive copying or publication of the theses in whole or in part also requires the consent of the Dean of the Graduate School of the University of Kentucky.

THESIS

Christopher James Morgan

The Graduate School

University of Kentucky

2004

MICRO ELECTRO-DISCHARGE MACHINING: TECHNIQUES AND PROCEDURES FOR MICRO FABRICATION

THESIS

A thesis submitted in partial fulfillment
of the requirements for the degree of
Masters of Science in Mechanical Engineering
College of Engineering at the University of Kentucky

By

Christopher James Morgan

Lexington, Kentucky

Director: Dr. R. R Vallance, Assistant Professor of Mechanical Engineering Department

Lexington, Kentucky

ACKNOWLEDGEMENTS

The author would like to sincerely thank Ryan Vallance at George Washington University for all of his guidance and assistance of this research. The author would also like to thank King Fu-Hii, I.S. Jawahir, Keith Rouch, and Scott Stephens at the University of Kentucky, Sergio Serrano at Temple University, Eric Marsh at Penn State University, and Manas Lakshmipathy at Zygo Corporation for their assistance in this research project. The author would also like to thank Takeshi Masaki and the Production Engineering Group at Matsushita Electric for their kindness and generosity in the author's trip to Japan in the summer of 2002, and assistance and support of the research conducted at the University of Kentucky.

TABLE OF CONTENTS

LIST OF TABLES

LIST OF FIGURES

LIST OF FILES

MicroEDM.pdf	7.1 MB

Chapter 1. Introduction and Thesis Overview

1.1. Introduction to the Micro Electro-Discharge Machining

Although micro electro-discharge machining is considered a relatively new technology, the groundwork for μ-EDM was laid in 1968 by Kurafuji and Masuzawa [1]. They were able to achieve a 6 μm hole in carbide block 50 μm thick with a process represented by Figure 1. During this process a conductive tool electrode and workpiece anode are connected to an RC circuit and submerged in a dielectic medium. As the tool electrode approaches the workpiece the impedance between the two becomes greater than the impedance in the capacitor. At this point a discharge occurs, which results in a plasma column between the anode and cathode.

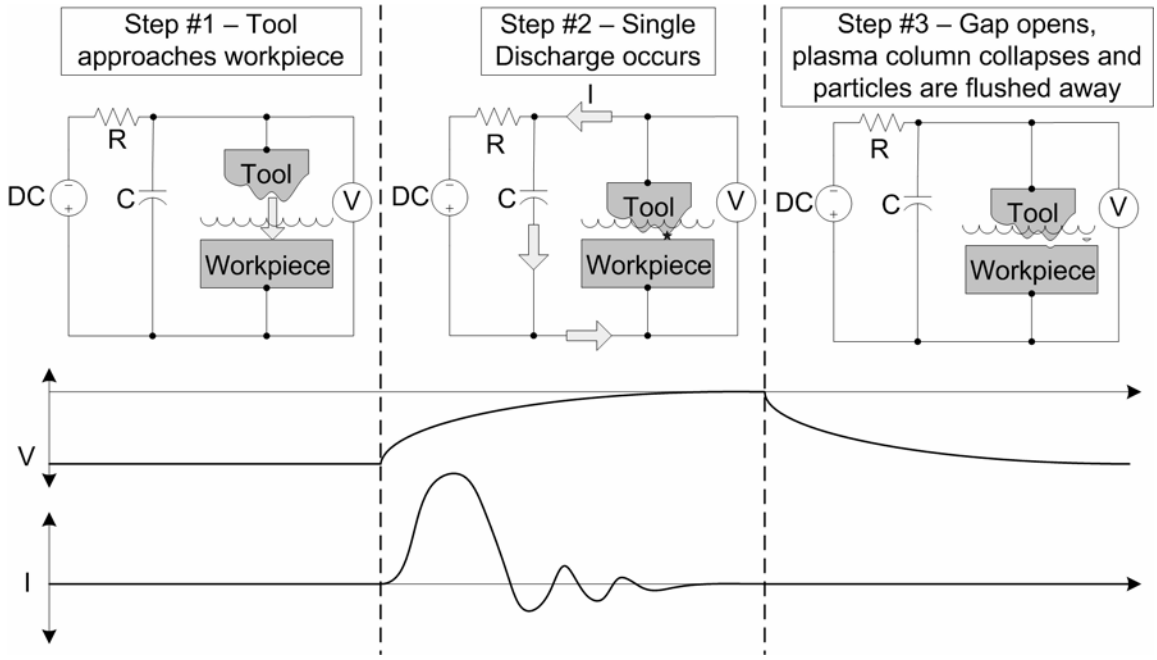

Figure 1. Relaxation (RC) circuit to achieve electro-discharge machining

The flux of electrons causes the cathode and anode to heat above their melting temperatures. The volume of material around the plasma column becomes molten and flows into the dielectric medium. The displaced material causes an increase in the gap, therefore the plasma column collapses and the molten particulate is flushed away. The discharges occur across a small gap (~ 2μm) filled with dielectric oil, which increases impedance and assists in

flushing the molten particulate out of the gap. As the pulses continue more material is removed from the cathode and the anode, replicating the shape of the tool electrode into the workpiece.

The technology grew rapidly and was introduced into production by Matsushita Electric Industrial Co., Ltd. through the research of Masuzawa and colleagues [2]. These machines are distributed world wide under the Panasonic name, product numbers MG-ED82W and MG-ED72W. In 2001 the University of Kentucky Precision Systems Laboratory purchased the MG-ED72W, see Figure 2, and research for this dissertation was performed on that machine.

The Panasonic machine is 3.5 axis machining center with a special controller to carry out electrical discharge and feedback. Feedback from the RC circuit is used to detect a short in the circuit. A short will occur when the material removal rate is not sufficient to keep up with the feed speed of the electrode towards the workpiece and contact is made. The controller detects the short and reverses the feed direction until the circuits is open again. The controller then reversed feed direction again and slowly begins feeding towards the workpiece again. Shorting the circuit is undesirable because the electrode or workpiece may be damaged and the machining time increases drastically. Feed rates should always be set such that shorting is rare or never occurs.

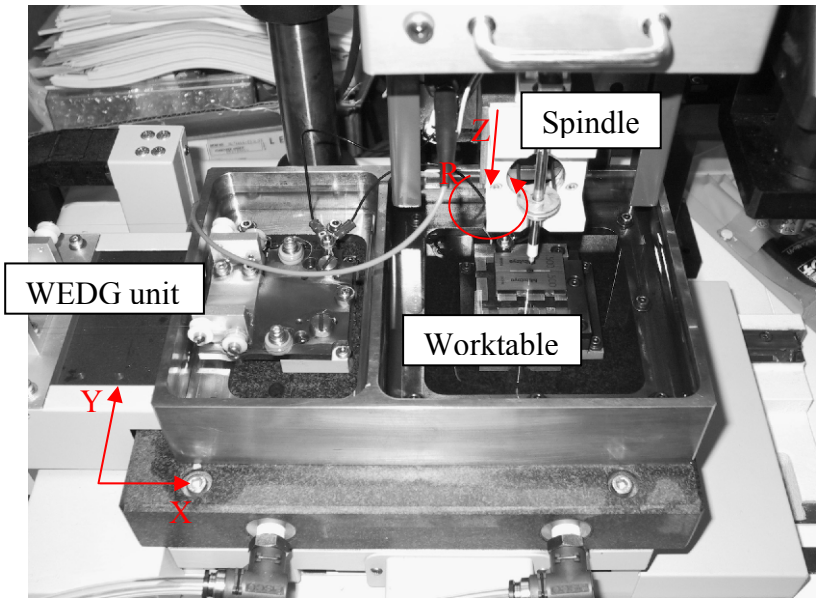

Figure 2. Panasonic Micro Electro-discharge Machine, MG-72

Electro-discharge machining (EDM) is well suited for micro machining high-strength conductive materials since neither mechanical contact nor cutting is necessary. Materials such as stainless steel and tungsten carbide are machined easily with electro-discharge and negligible cutting forces are applied to the tool or workpiece. The main disadvantage of electrical discharge is that during each discharge some material is removed from the tool. The melting temperature, conductivity, and change of yield stress due to temperature determine the wear rate of the tool and workpiece.

Techniques and procedures have been developed to compensate for the adverse wear effect on the tool. In 1985 Masuzawa [3] described a technique labeled Wire Electro-Discharge Grinding or WEDG. The WEDG method uses a moving brass wire as a cathode to erode away material from a rotating workpiece, producing a cylindrical shaft. Also Sato [4] described a method for drilling micro-scale holes using cylindrical electrodes. Since then, research on micro EDM has concentrated on either characterizing the process or applying the process to manufacture particular microstructures. Two applications of micro EDM include micro pipes/nozzles [5] and ink jet nozzles [6].

1.2. Wire Electro-Discharge Grinding (WEDG)

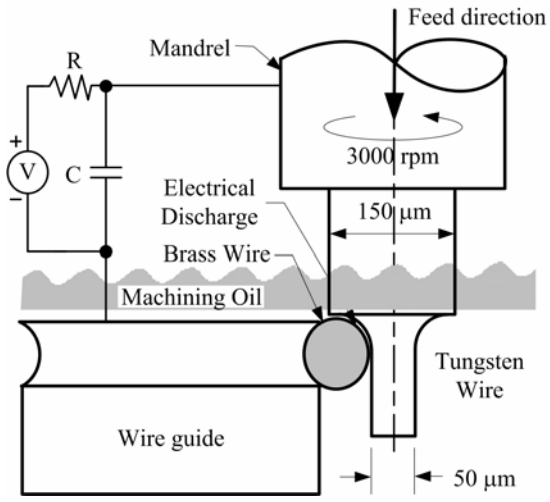

Figure 3. Wire Electro-Discharge Grinding

The WEDG process, illustrated in Figure 3, is similar to turning on a lathe. A simple RC circuit generates pulses that produce electrical discharges between the workpiece (anode) and a

φ100 μm brass wire (cathode). The discharges occur across a small gap (~ 2μm) filled with dielectric oil. The workpiece is held vertically in a mandrel that rotates at 3000 RPM, and its position is slowly fed in the z-direction. The wire is supported on a wire guide, and its position is controlled in the x- and y-directions. Each electrical discharge erodes material from the workpiece and the brass wire. To prevent discharges from worn regions of the brass wire, the wire travels at 340 μm/s, and is fed around a reel and take-up system as illustrated in Figure 4.

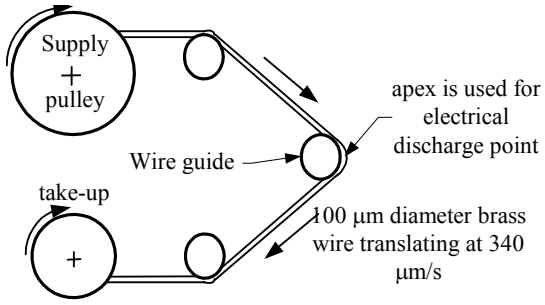

Figure 4. Traveling Wire in WEDG

Operation	Geometry	Process Conditions
Step 1: Flat End	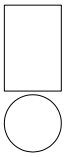	V = 100 V C = 1 Fh = 30 μm/s Fl = 2 μm/s
Step 2: Rough Cut	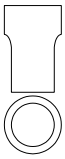	V = 110 V C = 1 Fh = 30 μm/s Fl = 3 μm/s
Step 3: Finish Cut		V = 70-80 V C = 4 Fh = 20 μm/s Fl = 30 μm/s

Figure 5. Typical Steps and Conditions for WEDG

A micro shaft is usually produced in three consecutive steps as illustrated in Fig 4. In the first step, the workpiece is positioned above the traveling wire, and the end of the shaft is machined by feeding the wire/guide in the x-direction. The second step is to rough cut the shaft and reduce the diameter of the stock material by feeding the workpiece in the z direction. A high material removal rate (MRR) is achieved during the rough cut by increasing the energy of each discharge, which depends upon the energy stored by the capacitor as given in Equation (1-1).

The final step is to finish cut the shaft. The voltage and capacitance are reduced to achieve improved form and surface finish. Although the multi-step process is based on the premise that improved precision is obtained by reducing the capacitance and voltage, a numerical relation for straightness or roughness is not available.

$$E = \frac{1}{2} CV^2 \qquad (1\text{-}1)$$

Substantial effort has concentrated on the precision of holes or cavities machined by micro EDM using cylindrical electrodes made by WEDG. Masuzawa et al. [7,8] used a vibroscanning method to measure holes drilled by micro EDM, and Yu et al. [9,10] developed the uniform wear method to reduce inaccuracy arising from electrode wear when micro-machining cavities. Yu et al. [11] later studied the influence of current, voltage, layer depth, and feed on the material removal rate, electrode wear ratio, and gap during contour milling with a cylindrical electrode.

1.3. Poly Crystalline Diamond (PCD) Grinding

Tool wear associated with micro-electro discharge machining can be a serious issue. The finished product in micro machining, whether it is a shaft or a hole, almost always requires a fine surface finish. The extra steps required to achieve a polished surface are not desirable for production components. Therefore, Matsushita Electric Industrial Co., Ltd. developed a technique for micro grinding using micro-edm trued diamond tools [12].

1.3.1. Poly Crystalline Diamond Tools

The diamond tools are made from polycrystalline diamond (PCD), which consists of small diamond grains sintered together under high temperature and pressures with 2-8% volume of metallic cobalt [13][14]. The cobalt fills the interstices between the diamond particles and forms an electrically conductive network of cobalt molecules. As a result PCD is an ideal candidate for electrical discharge machining. There are no forces during machining and the resulting PCD structure has high hardness and stiffness. Research has shown that PCD with finer grain structures are easier to machine and have higher grinding ratios and lower surface and

edge roughness [13][15]. For the research performed by Matsushita [12] and the research performed here at the University of Kentucky a PCD tool developed by Sumitomo Electric Industries, Ltd. (DA 200) is used. The tool is cylindrical in shape, 1mm in diameter, and has an average grain size of 0.5 micrometers.

The PCD tools fabricated with the WEDG unit on Panasonic micro-EDM are very useful for a finish cut during fabrication of conductive materials. But, at the elevated temperatures at the grinding zone, chemical reactions can occur between the diamond, workpiece material, binder, atmosphere, and fluid medium. For example, ferrous materials are not ideal due to the high tool wear rate resulting from a chemical reaction that occurs between the diamond particles and the iron in the workpiece [16]. During the summer of 2002 I visited the Panasonic Production Research facility located on the main campus for Matsushita Electric. During my two month stay I was introduced to many of the techniques and procedures explained in this thesis. I was also introduced to a technique termed "ductile mode grinding of brittle materials", which is a plastic deformation process that produces a polished surface with no surface or sub-surface damage [17]. The majority of my research with PCD tools deals with their application to ductile mode grinding of brittle materials and increasing the material removal rate during micro grinding.

1.3.2. Ductile Mode Grinding of Brittle Materials

As today's technology shrinks further and further in size it is important to develop novel techniques to fabricate complex micro parts. Precision machining of engineered ceramics is critical for applications, such as, automobile diesel injectors, magnetic heads for computers, semiconductor components, micro fluidic devices, and optical lens moulds [18]. These applications require form tolerances on the order of a micrometer and surface roughness values on the order of a nanometer, as well as temperature stability and high stiffness. Conventionally two steps are used to achieve the desired tolerances, grinding then polishing. The addition of the polishing step can be costly and time consuming; therefore ductile mode grinding of the brittle material is used to eliminate the polishing step [16].

A comprehensive investigation of ductile mode grinding of brittle materials yielded numerous papers specifically dealing with the use of PCD tools. In an effort to try and

understand why brittle materials become ductile during machining Bifano [19] discovered that a critical depth existed from which the grinding transitioned from ductile to brittle. The critical depth, which ranged from 100 nm to 400 nm, varied with material properties such as modulus of elasticity, E, and hardness, H. Bifano provided the following equation for the critical depth of cut:

$$d_c = 0.15\left(\frac{E}{H}\right)\left(\frac{K_c}{H}\right)^2 \tag{1-2}$$

Where K_c is a surface property constant. Bifano found the "critical depth" model had many difficulties, such as, the grain depth of cut is difficult to measure and the process variables such as cutting speed were not included. Bifano hypothesized that during ductile mode grinding the specific energy required to break the molecular bonds was constant, and a drastic decrease occurred when brittle grinding began. Bifano used this hypothesis to discover the specific energy required for certain materials. He used the results to generate feedback for in-process control of the transition from ductile to brittle grinding [17]. The equation for specific energy is:

$$\mu = \frac{P}{Q_w} = \frac{F_t \times v_w}{A_c \times v_w} = \frac{F_t}{A_c} \tag{1-3}$$

where μ is specific grinding energy, P is the power used during grinding, Q_w is the volumetric removal rate, F_t is the cutting force, A_c is the cross sectional area of the cut, and v_w is the workpiece speed.

Golini and Jacobs [20] showed that during microgrinding three phenomenon can be experienced; brittle, ductile, and smear mode. Smear mode grinding can occur when the diamond grains are small, on the order of a micrometer, or when the grinding tool becomes dull. Therefore, microgrinding can be a complex cutting process and many variables affect the resulting surface roughness, form, and subsurface damage. Interaction between diamond grains, the binder and the workpiece; and wear of the diamond can add to the complexity [21]. Cheng provided the following comprehensive chart for the factors affecting microgrinding.

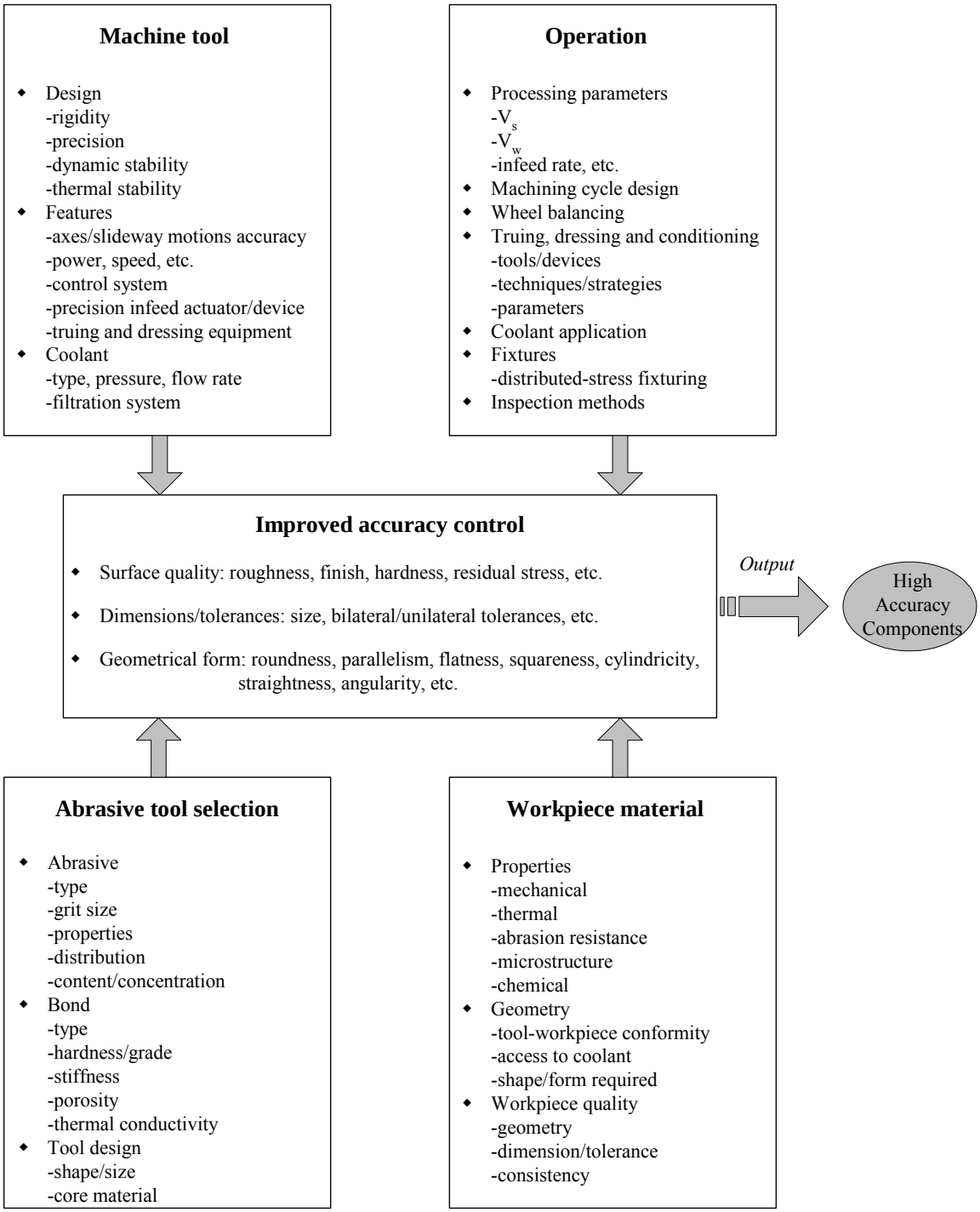

Figure 6. Parameters influencing microgrinding processes, adapted from [16]

1.4. Thesis Overview

This thesis describes the techniques and procedures used to fabricate micro components with micro electro-discharge machining. These components may be actual parts, or tools for further machining or molding. In order to understand the limitations and capabilities of this process experiments are designed to explore and optimize the machining parameters utilized in micro fabrication of complex three-dimensional microstructures. The hypothesis for this thesis is stated below.

1.4.1. Thesis Hypothesis

Micro electro-discharge machining is a precision machining technology that is capable of fabricating complex three-dimensional microstructures in conductive workpieces. Micro electro-discharge machining can also be used to fabricate poly-crystalline diamond tools that can subsequently be used for ductile mode grinding of brittle materials such as glass and silicon. The accuracy, precision, and material removal rates make these micromachining techniques a viable resource for the future of micro and nano technologies.

1.4.2. Thesis Contents Overview

Chapter 2 is an introduction to the WEDG process. The precision of microshafts will be analyzed in order to optimize machining parameters. Chapter 3 describes micro machining processes using the microshafts for further electro-discharge machining of simple geometries, such as, holes and slots. Chapter 4 is a description of ductile mode grinding of brittle materials using poly-crystalline diamond tools. And finally, Chapter 5 contains applications, such as parts and tools machined with the techniques described in this thesis.

Chapter 2. Precision of Micro Shafts Machined with WEDG

2.1. Introduction to the Chapter

Wire electro-discharge grinding (WEDG) is a micro fabrication process that uses electrical discharges in a dielectric fluid to erode material from conductive wires and produce micro shafts. A typical tungsten micro shaft produced with WEDG is illustrated in Figure 7; the diameter and length are approximately 50 μm and 1.5 mm, respectively. These shafts are finding increasing application in microstructures and as tools in subsequent micro fabrication processes. For instance, cutting tools produced with WEDG were recently used to drill holes in silicon [22], and grinding wheels were made from polycrystalline diamond [12].

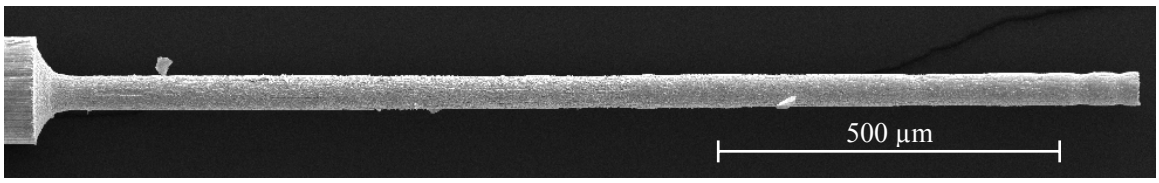

Figure 7. Micro shaft produced with WEDG

In these applications, the accuracy and precision of the micro shafts produced by WEDG are crucial for achieving accuracy and precision in the subsequent processes. However, it is visually evident in Figure 7 that surface defects and variation in the diameter of the shaft exist. Despite this, studies have not related process conditions during WEDG or machine errors to the precision or accuracy of micro shafts. Therefore, the objective of this work was to measure the variation in a set of micro shafts and subsequently relate the variation to process conditions and machine errors.

This chapter presents the fabrication and metrology of 81 micro shafts produced with various process conditions. The sensitivity of the shafts' roughness and straightness is assessed with statistical box plots. The analysis reveals the precision of the WEDG process. Furthermore, the results suggest that the roughness of the shaft depends mainly upon process conditions, and the straightness appears to be dominated by machine and process errors. An error model and an analysis of variation support this conclusion.

2.2. Fabrication of Micro Shafts

Tungsten micro shafts are produced by WEDG using the Panasonic MG-ED82W micro EDM machine (see Figure 8), patented by Masaki et al. [23]. The stock tungsten wires (ϕ 150 μm) are machined down to a nominal diameter of about ϕ 50 μm with a single cut. Three different lengths are manufactured to achieve aspect ratios (L/D) of approximately 10, 20, and 30.

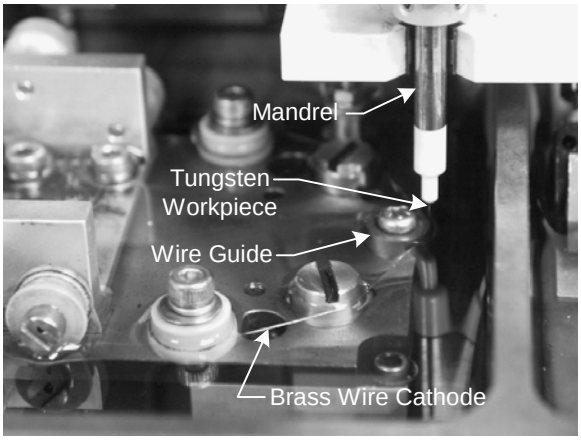

Figure 8. Panasonic MG-ED82W micro EDM machine, WEDG setup

The process variables for this experiment are voltage (V), capacitance (C), and feed rate of the tungsten workpiece. The values of each variable (Table 1) are chosen based on machine capabilities and experience. For each shaft a computer program is written to control the variables and record the time of machining. 81 shafts are machined to cover all possible combinations of the variables.

Table 1. Summary of Experimental Variables

Voltage, V	70, 80, 100
Capacitance, pF	10, 220, 3300
Feed Rate, μm/s	1, 3, 5
Shaft Length, μm	500, 1000, 1500
Shaft Diameter, μm	50

2.3. Metrology of Micro Shafts

After machining each micro-shaft is cleaned in an ultrasonic cleaner and the edge profile is measured with a 3D surface profilometer (Zygo NewView 500). The profilometer has ultra fine height resolution (sub-nanometer), which makes it acceptable for surface roughness and straightness measurements. The CCD camera was set to 640x480 resolution, and a 10x objective was used. This provided a lateral resolution of 0.64 μm.

Sample 3D data acquired for a single shaft is plotted in Figure 9. The scan region was typically about 20 μm wide and equal to the machined length. 2D profiles are obtained from the 3D data by selecting a scan line, drawn over the length of the shaft in the x direction. The 2D profiles have repeatable form error across a wide region of the scanned data; therefore precise placement of the scan line is not necessary. Each micro shaft is scanned twice at random locations around the circumference of the shaft.

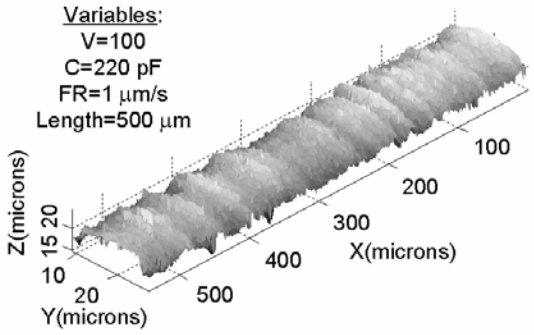

Figure 9. 3D Scan of Shaft Surface Acquired with Zygo NewView 500

After measuring all shafts with the profilometer, the data is analyzed with a Matlab script that determined straightness and roughness. The first step is to filter the data with a low-pass fft filter and separate waviness form errors from shaft roughness [24]. Standard wavelengths for separating these components are not available for micro shafts, therefore a spectral analysis was performed on the profile data, but dominant wavelengths were not apparent. A 10 μm cutoff wavelength is chosen based on visual observation of the profiles. A roughness profile is obtained by subtracting the filtered profile from the raw profile. The average roughness of each shaft, R_a, can be calculated using Equation (2-1) and data points, Z_i, from the roughness profile.

$$R_a = \frac{|Z_1| + |Z_2| + |Z_3| + \ldots + |Z_N|}{N} \tag{2-1}$$

The straightness of each shaft is determined from the raw profiles by a method similar to that described by Weber et al. [25]. A least-squares line like the one shown in Figure 10 is calculated by minimizing the squared deviations of the orthogonal distance (d_i) between the line and the raw profile. The least-squares straightness tolerance (S) is then calculated using Equation (2-2) as the difference between the minimum and maximum distances.

$$S = \max(d_i) - \min(d_i) \tag{2-2}$$

The shafts and measurements shown in Figure 11 illustrate the range of values observed for roughness and straightness. In general, the SEM images correlate well with the measured profiles.

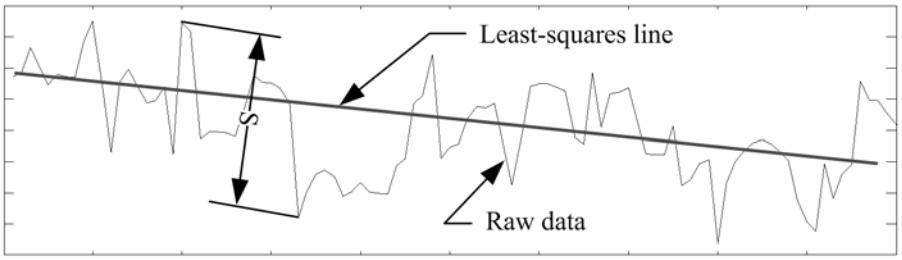

Figure 10. Visual explanation of straightness calculation

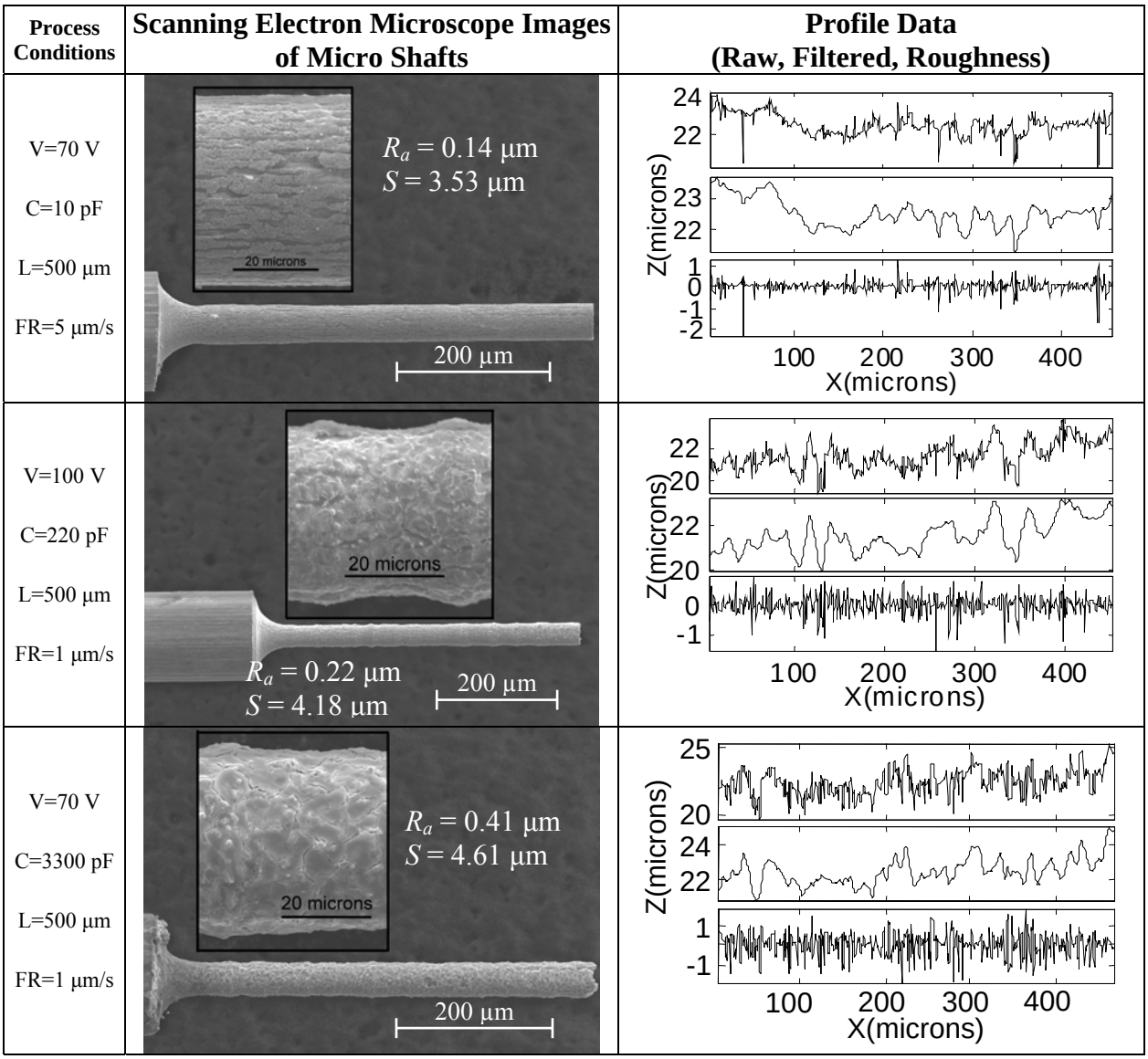

Figure 11. Range of Roughness and Straightness Measured using 2D Profiles of Micro Shafts

2.4. Sensitivity Analysis

The straightness and roughness of the micro shafts are grouped into categories and plotted on statistical box plots. An ANOVA analysis is performed on each group to test the hypothesis that the data is from same population or that one treatment is different from the others [26]. At the 5% level of significance, Figure 12 shows that R_a is independent of feed rate and aspect ratio. As expected, R_a is dependent on voltage and capacitance. It was expected that surface roughness should increase with capacitor energy, but mean comparison tests suggest that the lowest surface roughness can be achieved with a capacitance of 10 pF, and a voltage of 80.

Therefore surface roughness does not decrease with discharge voltage and an optimal value exists.

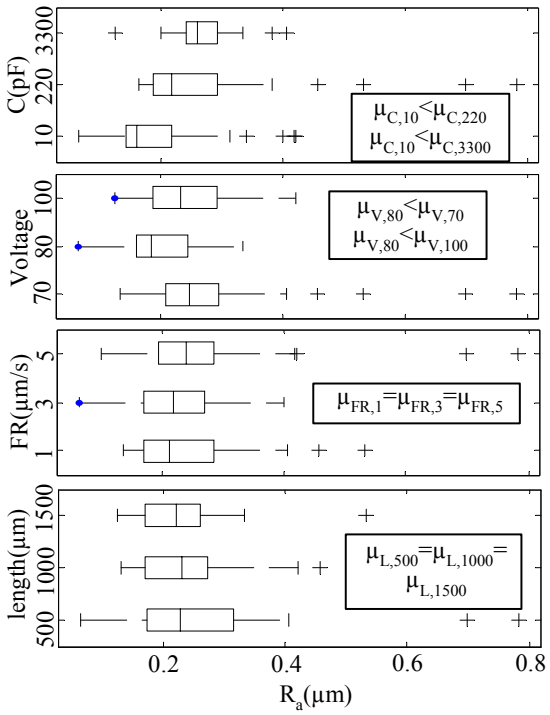

Figure 12. Box Plots of variables versus micro shaft R_a, and mean comparison results using a 5% statistical level of significance

Figure 13 shows that straightness is independent of voltage, capacitance, and feed rate. But, as the length of the shaft increased, straightness errors are increased. This indicates that machine errors likely dominate the straightness of the micro shafts.

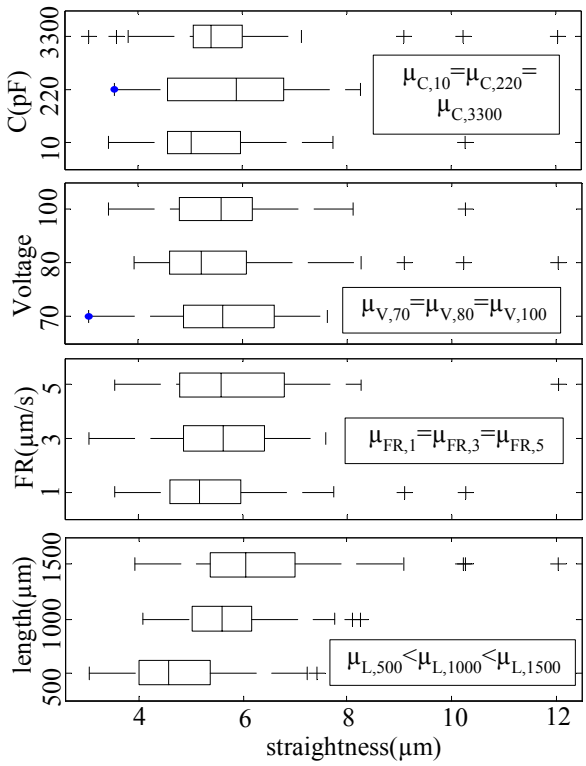

Figure 13. Box Plots of variables versus straightness, and mean comparison results using a 5% statistical level of significance

2.5. Model of Process and Machine Errors

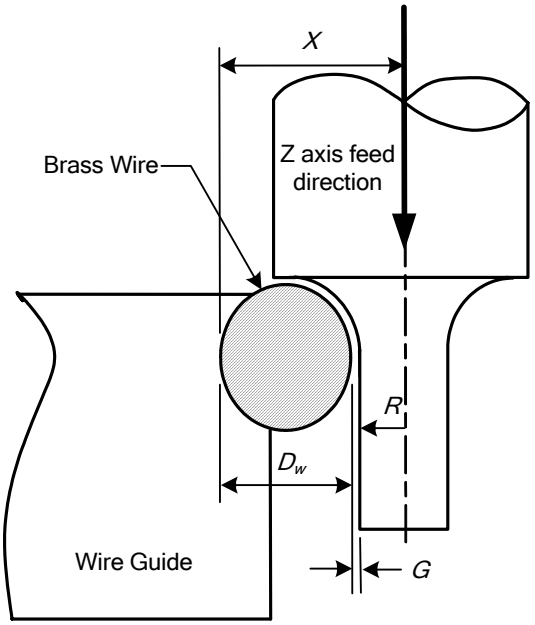

Figure 14. Errors in WEDG Process

Machine errors during the WEDG process likely produce form errors in the micro shafts. Therefore, errors in the sensitive direction are modeled as shown in Figure 14. The straightness of edge profiles is essentially variation in shaft radius. The radius of the shaft, R, depends upon the relative position between the wire guide and workpiece, X, diameter of the wire, D_w, and gap, G, as given in Equation (2-3).

$$R = X - D_w - G \tag{2-3}$$

Assuming these are continuous and independent random variables, then the variance in R is simply the sum of the variances in X, D_W, and G as given in Equation (2-4).

$$\sigma_R^2 = \sigma_X^2 + \sigma_{D_w}^2 + \sigma_G^2 \tag{2-4}$$

The variance in X is a primarily a combination of error motion in the machine's z-axis, spindle radial error motion, and thermal drift and is given by Equation (2-5).

$$\sigma_X^2 = \sigma_{z-axis}^2 + \sigma_{thermal}^2 + \sigma_{radial}^2 \tag{2-5}$$

The variance in the gap is difficult to measure and is assumed negligible. Substituting Equation (2-5) into Equation (2-4) provides an expression for σ_R^2.

$$\sigma_R^2 = \sigma_{z-axis}^2 + \sigma_{thermal}^2 + \sigma_{radial}^2 + \sigma_{D_W}^2 \tag{2-6}$$

Experiments are designed to determine each component in Equation (2-6). Summing these components will result in the variation in the sensitive direction and this value should correlate with the variation in the measured shaft profiles.

2.5.1. Z-Axis Error Motion Analysis

The z-axis error motion is measured with the reversal technique described in [27]. For this experiment the spindle shaft serves as the gauging surface and a lion precision capacitance gage is used to measure the displacement of the shaft. The z-axis is incremented downward and a profile is acquired, *N(z),* which represents the motion of the z-axis carriage and the form error of the shaft. To remove the form error in the shaft *S(z)*, the capacitance gage and spindle shaft are rotated 180° and another profile is acquired, *R(z)*, see Figure 15. The real motion, *M(z)*, of the z-axis carriage can be calculated using Equation (2-7).

$$M(z) = \frac{N(z) - R(z)}{2} \tag{2-7}$$

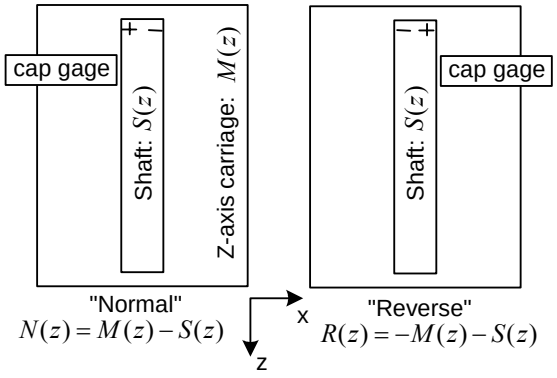

Figure 15. Z-axis error motion experimental setup and equations

Figure 16 is a plot of the measured profiles. The standard deviation of the z-axis carriage motion, *M(z)*, is calculated to be 135 nm.

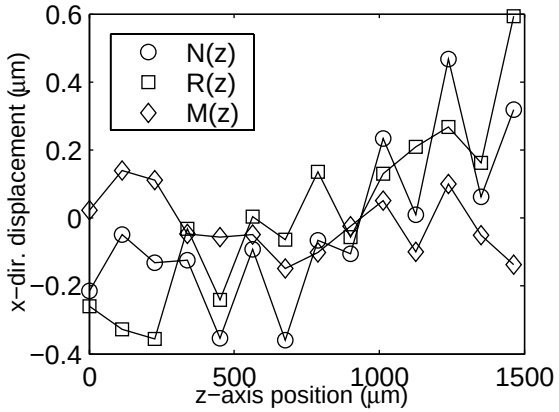

Figure 16. Plot of z-axis error versus position; normal, reverse, and carriage profiles

2.5.2. Thermal Drift Analysis

Thermal drift in the machine carriage is measured with the setup shown in Figure 17. Two capacitance gages are placed on concentrically on either side of a gage block that is held on the z-axis carriage. The drift of the gage block is recorded over 36 hours and displacements of gages are averaged to eliminate the effect of thermal expansion of the gage block. The averaged displacement is plotted in Figure 18 and the resulting standard deviation is 164 nm.

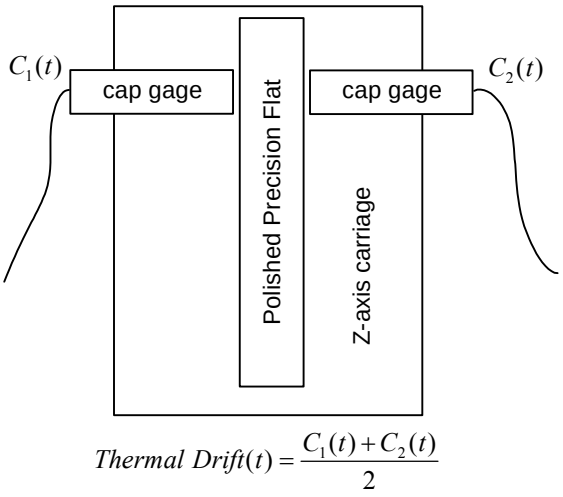

Figure 17. Thermal drift experimental setup and equations

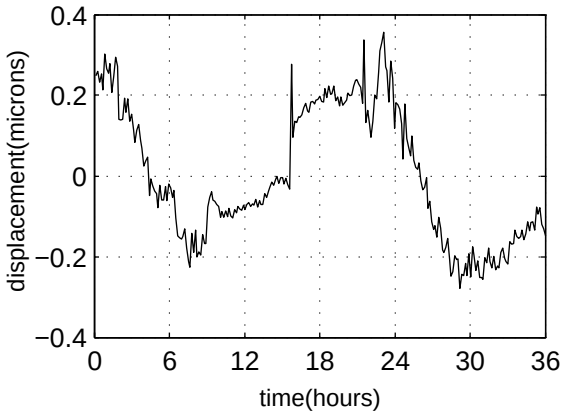

Figure 18. Plot of thermal drift versus time over 36 hours

2.5.3. Radial Error Motion Analysis

To measure the radial error motions, a 512 count encoder wheel with read head was placed on the spindle shaft, see Figure 19. A lion precision contact probe is used to measure the spindle displacement at each angular position. The reversal technique is used again to eliminate the influence of the shaft form error.

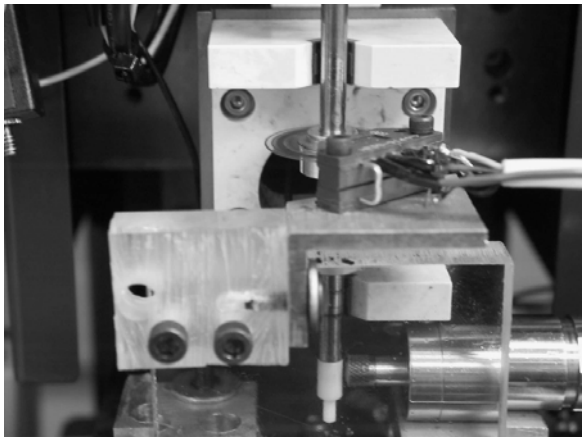

Figure 19. Radial error motion experimental setup

Figure 20 is a polar plot of the radial error motion and a Fourier Transform Analysis of undulations per revolution (UPR). The first UPR has been removed to center the data and the resulting data displays a predominately two lobed error motion. The synchronous error and the asynchronous error are calculated to be 588 nm and 154 nm, respectively. Synchronous error motion will cause roundness form errors and asynchronous error motions will cause roundness

and straightness form errors, therefore for this investigation only asynchronous error motions are considered. Figure 21 is a histogram of asynchronous error; the standard deviation is 28 nm.

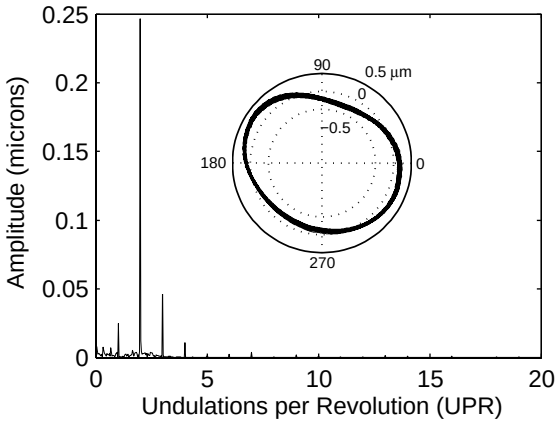

Figure 20. Radial error motion measured in sensitive direction

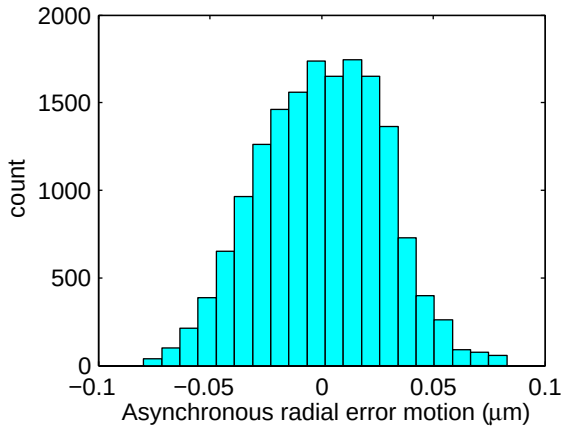

Figure 21. Histogram for asynchronous error motion

2.5.4. Cathode Wire Diameter Variation Analysis

The cathode wire is placed in a precision vee-groove and a lion precision capacitance gage is used to measure the variation of the wire diameter, see Figure 22. The cathode wire is "pulled through" the vee-groove and measurements are taken at random locations along the length of the wire. Figure 23 is a histogram of the variation measurements, and the standard deviation is 721 nm.

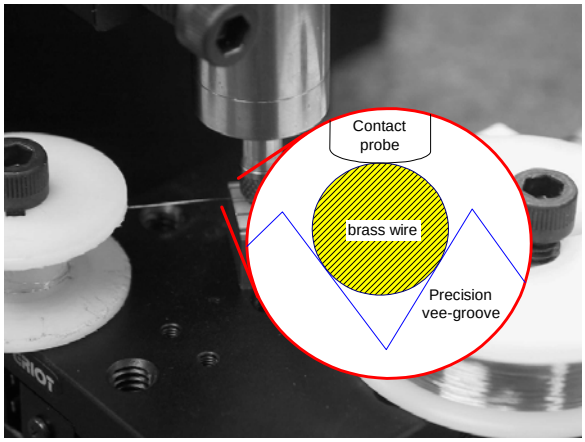

Figure 22. Wire diameter variation experimental setup

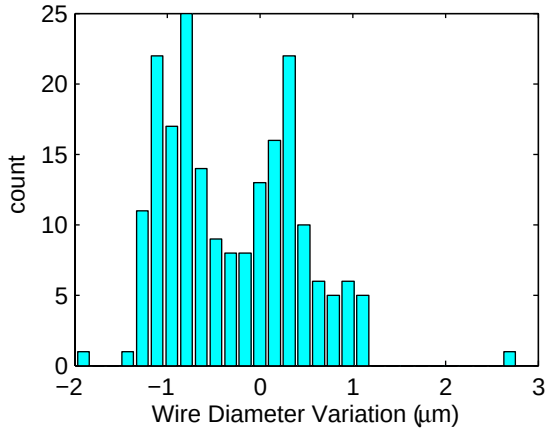

Figure 23. Histogram of wire diameter variation

2.5.5. Summary of Process and Machine Errors

Table 2 lists a summary of the standard deviations and 95% confidence intervals for the measured error sources, and the predicted standard deviation of the micro shafts radius. The variance of the wire diameter dominates the machine and process errors since it is an order of magnitude above the other error sources and the roughness values.

Table 2. Process Errors and Predicted Variation in Radius of Micro Shaft

Error Source	Standard Deviation & 95% Confidence Intervals		
	Lower Limit (μm)	Std. Dev. (μm)	Upper Limit (μm)
Z-axis	0.1181	0.1351	0.1561
Thermal	0.149	0.1644	0.181
Radial	0.0273	0.0276	0.0279
Wire (D_W)	0.655	0.726	0.797
Radius, *R*	**0.683**	**0.757**	**0.833**

The results of the error model suggest that σ_R should lie between 0.683 and 0.833 μm. To verify this hypothesis the filtered micro shaft profiles (excludes roughness) are used to calculate the standard deviation of the entire population. The standard deviation of the distances, d_i, from the least-squares line is found to be σ_d=0.823 μm. This value is within the predicted standard deviation interval and implies the dependence of edge straightness on machine/process errors rather than process variables.

2.6. Optimal Parameters for Maximum Material Removal Rate and Minimum Surface Finish

From the statistical analysis of the shafts it was concluded that low discharge energy is optimal for achieving minimum surface roughness. Figure 24 is a plot of material removal rate (MRR) versus the energy per discharge, for each shaft. An overall trend is observed that as the energy per discharge increases the MRR increases. Therefore, machining time is the limiting factor for achieving minimum surface roughness.

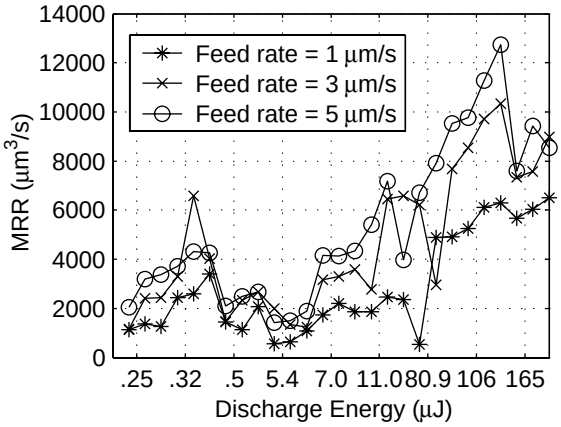

Figure 24. Dependence of Material Removal Rate on Discharge Energy

To improve material removal rate a two-step process is presented. In the first step the micro shaft is rough-cut with a high discharge energy and, therefore, high MRR. In order to prevent machining on the finished surface, the rough cut should have a diameter of the finish diameter plus six times the standard deviation measured from the error model. Finally, a finish pass with capacitance of 10 pF and voltage of 80 will produce a micro shaft with minimum surface roughness. To verify this hypothesis a micro shaft is fabricated with the procedure described above. A micro shaft with high MRR, 8855 $\mu m^3/s$, and R_a of 194 nm is achieved.

2.7. Achievable Aspect Ratio

The WEDG process is non-contacting therefore high aspect ratio shafts are achievable. The limiting factor is the force applied to the tungsten wire during fabrication of the shaft. The only forces experienced during fabrication are the electrostatic forces due to the plasma column that occurs during discharging and the forces due to vibration of the electrode during rotation. To check for failure due to electro-discharge forces, the worst-case scenario is assumed, see Figure 25. During the WEDG process a discharge could occur at the very tip of the tungsten wire during the spark-out period. The spark-out period occurs when the shaft is finished machining and the polarity is reversed and the electrode is withdrawn above the brass wire. Assuming a discharge occurs at the tip of the shaft and the highest discharge energy is applied, 100 Volts and 3300 pF of capacitance, the force due to a single discharge is calculated.

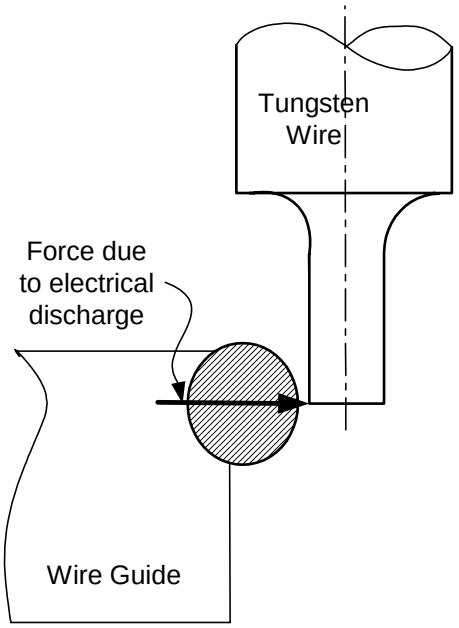

Figure 25. Diagram of electrostatic force that could occur during the WEDG process

Singh and Ghosh [28] showed that using a thermo-electric model the surface stress due to a single discharge could be written as:

$$\sigma = \frac{2I}{\pi R^2}\sqrt{\frac{-2m_i\phi_w}{e}} \tag{2-8}$$

where; I is the current, R is the discharge radius, m_i is the mass of an ion, φ_w is the voltage potential, and e is the electronic charge (1.6×10^{-19} Coulomb). The following assumptions [28, p. 671] were made in the derivation of equation (2-8):

1. The electrode (brass wire) is a semi-infinite zone.
2. The spark is a uniform, circular heat source on the electrode surface and the diameter of this source is a constant.
3. Except for the yield strength, the properties of the material do not change with temperature.
4. The rate of heat input remains constant throughout the discharge time.
5. The plasma region acquires the potential of the anode and the whole potential drop is in the sheath near the cathode and the plasma region near the sheath. The plasma potential is

actually governed by the positive potential and differs only slightly from it (Clauser, p. 58[29]).

6. The metal yields at the end of the discharge.
7. In the spark channel, there is no variation in the potential, ion and electron densities and the ion velocity in the radial direction.

To substitute the values into equation (2-8) that constitute our system, the current and mass of the ion must be evaluated. To discover the current a Tektronix CT-1 current probe was placed on the micro EDM machine during machining. The results of this experiment are contained in Appendix B. The maximum current during a single discharge was found to be 1 Ampere. The mass of the ion must be calculated from the ions that occur in the medium. The dielectric oil is a saturated hydrocarbon; therefore the dominating ion will be carbon. The mass of a carbon atom is 12 amu. The absence of the electron is ignored because the mass of an electron is negligible. To find the force on the tungsten wire, the stress is multiplied by the discharge area. The resulting equation is:

$$P = 2I\sqrt{\frac{-2m_i\phi_w}{e}} \tag{2-9}$$

The values are substituted into this equation and the force is found to be 0.01 μN, see Appendix C for a detailed calculation. The maximum stress of a circular beam in bending can be written as:

$$\sigma_{\max} = \frac{32PL}{\pi d^3} \tag{2-10}$$

Where L is the length and d is the diameter. Substituting the ultimate strength for $\sigma_{\max}$ and setting aspect ratio (ar) equal to L/d, an equation for the maximum aspect ratio with respect to electrode diameter is achieved.

$$ar_{\max} = \frac{\pi\sigma_{\text{ult}}d^2}{32P} \tag{2-11}$$

The ultimate strength of tungsten is 1400 MPa. Substituting known values into this equation yields equation (2-12)

$$ar_{\max} = 1.37 \times 10^{10} d^2 \qquad (2\text{-}12)$$

Figure 26 is a MathCAD graph of equation (2-12). The (x) data points represent aspect ratios achieved with the Panasonic micro EDM machine. The data points at 100 micrometers and 140 micrometers are not optimized due to spatial limitations. For example, the achievable shaft length for a 140 micrometer diameter should be 39 millimeters, but the Panasonic machine can only machine electrodes up to 12 mm long due to spatial limitations in the cutting tank. Electrodes below 50 micrometers achieve aspect ratios higher than predicted, but the discharge current used to machine these electrodes was much lower than the current used for the analytical analysis.

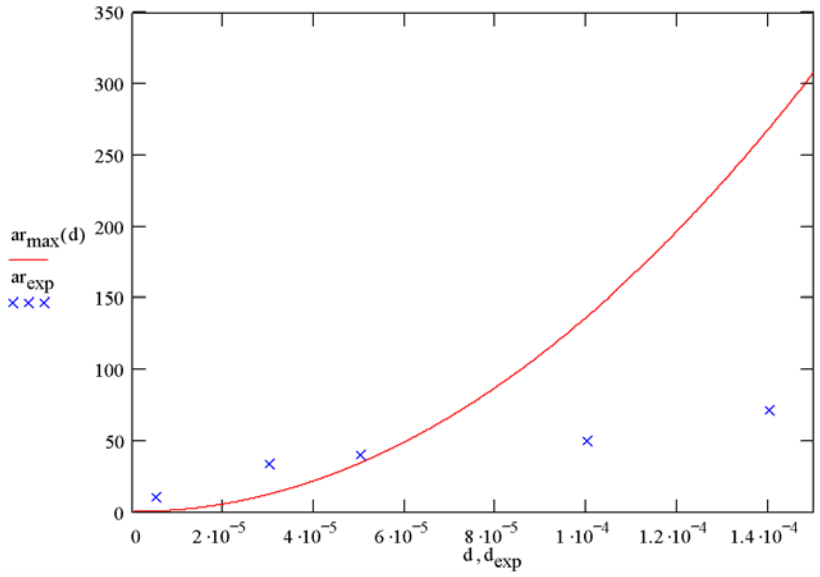

Figure 26. Maximum aspect ratios, calculated analytically and achieved experimentally

2.8. Chapter Summary

This chapter reports the precision of micro shafts manufactured with wire electro discharge grinding (WEDG). The precision was assessed by measuring the roughness and straightness of edge profiles for 81 shafts, machined with various process conditions. The average surface roughness, R_a, varied between 0.067 and 0.781 µm and depended upon capacitance and voltage. The straightness varied between 3.05 and 12.04 µm but was independent of all process conditions except aspect ratio. Straightness variation corresponded

well to the predicted variation in shaft radius as determined by combining variation in machine errors and the diameter of the anode wire. A two-step process is presented and a micro shaft with high MRR and low surface roughness is achieved.

The maximum shaft aspect ratios achievable on the Panasonic MG-ED72W machine are researched. It is found that the maximum shaft aspect ratio varies parabolically with the shaft diameter and very high ratios are possible with diameters over 100 micrometers. Experimental analysis is limited due to machine capacity, but trends support the analytical analysis.

Chapter 3. EDM: Techniques and Procedures to Achieve Micro Structures

3.1. Introduction to the Chapter

The precision micro shafts fabricated with the WEDG process in Chapter 2 can now be used for further electro-discharge machining. Pure tungsten wire is chosen for the tool material due to its high melting temperature. This produces a high "G ratio", which is defined as the material removal rate of the workpiece divided by the material removal rate of the tool. The accuracy, surface finish, and material removal rate of the machined cavity will depend on two main parameters; workpiece material and discharge energy. The higher the discharge energy the faster the material removal rate, but higher temperatures at the machining zone increase tool wear and produce a rougher surface. Lower discharge energies reduce the material removal rate, but the tool wear is small and the surface is smooth. The procedure to achieve accurate smooth cavities for simple and complex shapes is described in the following sections.

3.2. Hole and Slot Machining

3.2.1. Hole Accuracy

When a hole is machined using electrical discharges, some tool wear occurs on all surfaces in close proximity to the workpiece. The wear generates a conical shaped tool, see Figure 27. The resulting hole is tapered and the top of the hole is larger than the bottom of the hole. The angle of the taper and the resulting radius at the bottom of the tool will be a function of the discharge energy. Provided with the Panasonic micro-EDM machine is a chart of recommended machining conditions, Figure 28. Two machining conditions are provided, rough and high accuracy. The feed rate for the rough machining condition is consistently higher than for the high accuracy machining conditions.

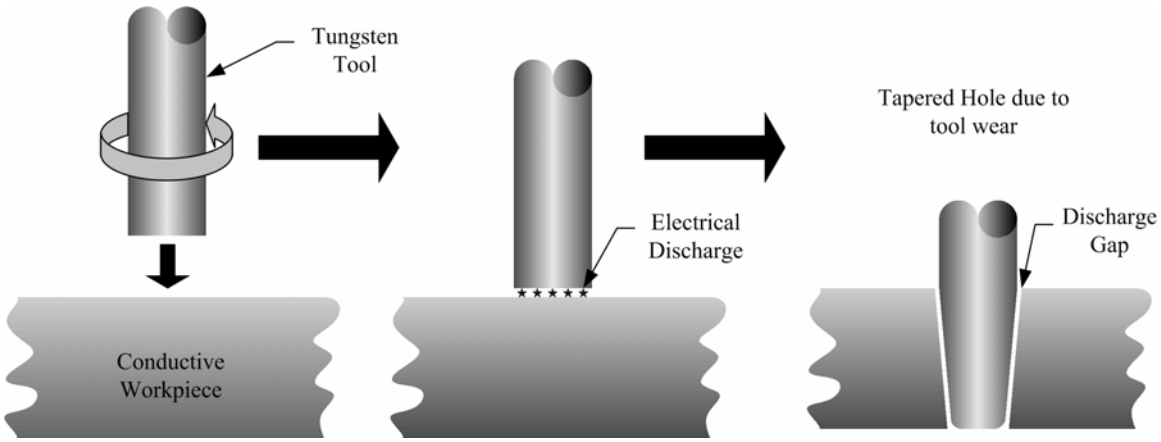

Figure 27. Hole drilling and resulting tool wear

Hole Shape			Tool Electrode Shape		High Accuracy Boring Condition					Rough Machining Condition				
Dia-meter D (μm)	Thick-ness (μm)	Number	Dia-meter	Length (μm)	Volt-age (V)	Capa-citor	Feed Rate L(μm/s)	Feed Rate H(μm/s)	Depth (μm)	Volt-age (V)	Capa-citor	Feed Rate L(μm/s)	Feed Rate H(μm/s)	Depth (μm)
10-30	T	n	D - 2.6	T x 2.5 + (n-1) x T x 0.1+ 50	70	4	1	15	T x 2.5	100	3	2	20	T x 2
25	75	1	22.4	250	70	4	1	15	188	100	3	2	20	150
15	20	40	12.4	180	70	4	1	15	50	100	3	2	20	40
31-50	T	n	D-2.6	T x 2.5 + (n-1) x T x 0.12+ 50	75	3	2	30	T x 2.5	100	2	4	50	T x 2
40	200	1	37.4	550	75	3	2	30	500	100	2	4	50	400
35	100	48	32.4	864	75	3	2	30	250	100	2	4	50	200
51-80	T	n	D-3.0	T x 2.5 + (n-1) x T x 0.15+ 50	80	3	2	30	T x 2.5	100	1	5	50	T x 2
75	350	1	72	925	80	3	2	30	875	100	1	5	50	700
55	100	100	52	1785	80	3	2	30	250	100	1	5	50	200
81-120	T	n	D-4.0	T x 2.5 + (n-1) x T x 0.2+ 50	100	2	2	30	T x 2.5	110	1	4	50	T x 2
100	500	1	96	1300	100	2	2	30	1250	110	1	4	50	1000
82	150	24	78	1115	100	2	2	30	375	110	1	4	50	300
121-300	T	n	D-6.0	T x 2.5 + (n-1) x T x 0.25 + 50	100	2	1	30	T x 2.5	110	1	3	50	T x 2
250	1000	1	194	2550	100	2	1	30	2500	110	1	3	50	2000
300	500	5	294	1800	100	2	1	30	1250	110	1	3	50	1000

Figure 28. Chart provided with Panasonic micro-EDM machine [30]

For most applications a two-step process can be used to provide high accuracy holes with a high material removal rate. Two tools are prepared; the rough cut is performed with one tool, the tool is replaced, and the second tool performs the finish cut. This method was used to achieve hole in a tungsten carbide, see Figure 29. In the case where tapered holes are desired, very small diameters can be achieved for the bottom of the sheet, see Figure 30. The radius of the entrance holes on the top surface is 5 μm, but the exit holes on the bottom have a radius as small as 0.5 μm.

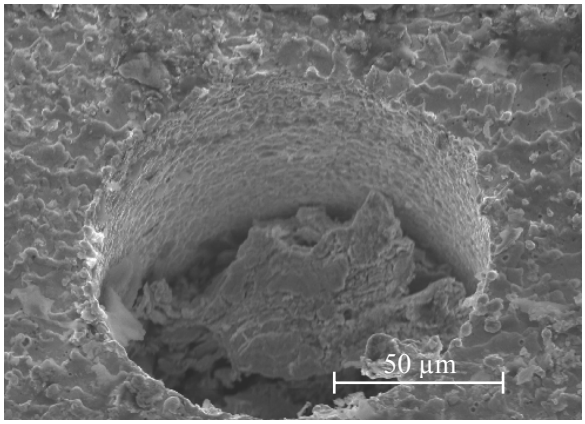

Figure 29. Holes drilled through a tungsten carbide sheet

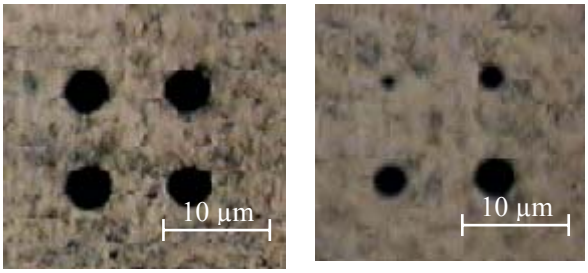

Figure 30. Four holes machined in brass sheet, top and bottom

3.2.2. Slot machining

Due to the high wear rate of the tungsten tools during hole drilling a new method was devised by Panasonic to control the location of the wear. If all discharging occurs at the end face of the electrode, the tool would shorten but retain the cylindrical shape. If the depth of cut is small but the feed speed is fast, efficient slot machining can be achieved. Figure 31 represents the tool path for slot machining. The tool feeds slowly downwards while vibrating parallel to the slot direction. The bottom of the slot will have a gradual slope, but if the vibration speed is sufficiently fast, the slope will be negligible. Figure 32 is a Scanning Electron Microscope image of a slot machined in aluminum. The radius at the bottom edge of the groove is on the order of 2.5 micrometers. The slot machining method was used to machine the UK symbol shown in Figure 33.

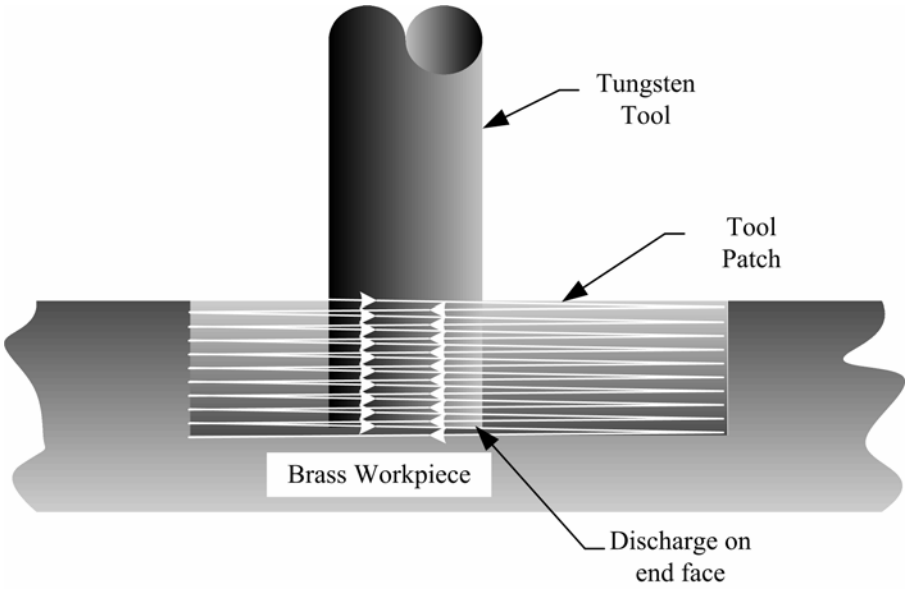

Figure 31. Tool path for slot machining

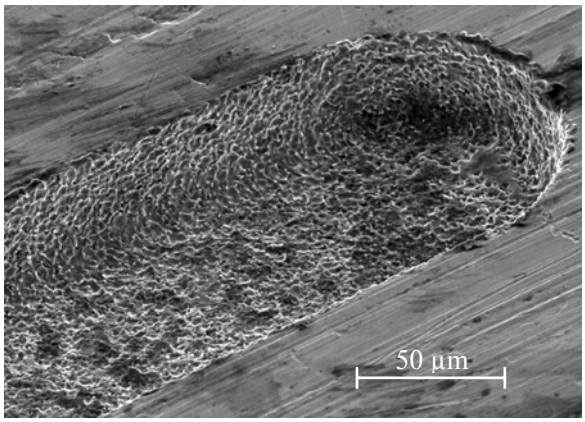

Figure 32. Slot Machined in aluminum, Capacitance 100 pF, Voltage 80.

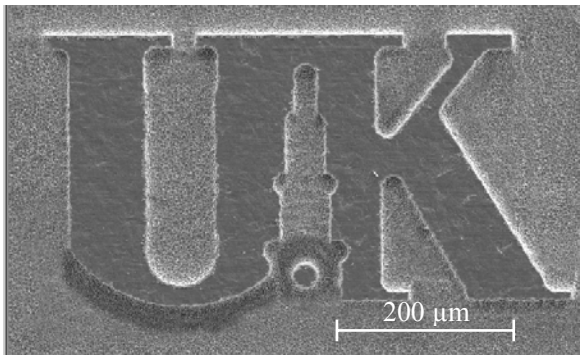

Figure 33. University of Kentucky logo machined with µ-EDM

3.3. Uniform Wear Method

The principal of discharging from the end face was used by Masuzawa to develop the uniform wear method [9]. Masuawa stated that if a small depth of cut was used and a tool path was chosen that crossed over the previous path by the radius of the tool, the majority of the wear would occur from the end of the tool. If the tool path is long the tool will be significantly shorter at the end of the path, therefore the next pass is reversed in order to achieve a flat substructure. See Figure 34 for an example of a process to machine a rectangular micro cavity.

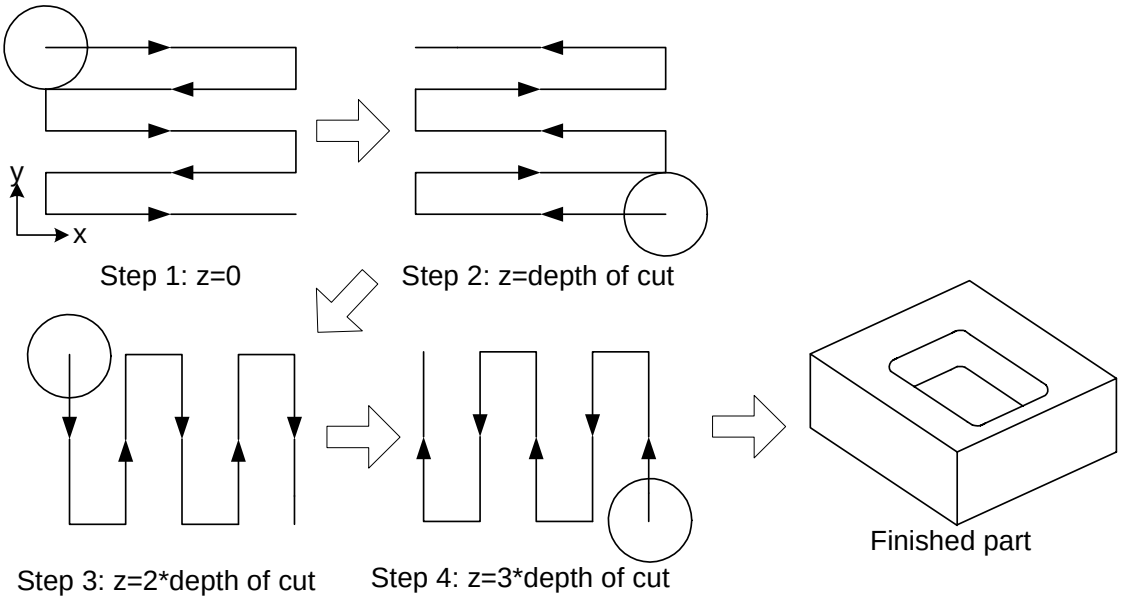

Figure 34. Description of tool path for uniform wear method

3.4. In Process Tool Dressing

Concentric cavities such as cylinders and cones are not efficient to machine with the uniform wear method due to the curved tool paths. A single tool is simpler and more robust method for machining such cavities. But, tool wear is a serious issue if multiple holes of the same size are desired. "In Process" tool dressing between each cavity will keep the tool "true" and precise. A polished sheet is used as the dressing tool and the area of the sheet used for each dressing is sacrificed. The specifics of precision cylinder and cone fabrication are contained in the following sections.

3.4.1. Precise Cylinder Fabrication

Precision cylinder truing is a very simple process. A vertical polished block, usually tungsten carbide, is oriented parallel to the rotation axis of the spindle. The rotating workpiece is advanced towards the sheet from the side. Once discharge occurs the sheet vibrates horizontally so the surface roughness is averaged out, see Figure 35. Only a few micrometers of material should be removed to prevent excessive wear of the polished block, which will result in radiusing at the tip of the tool. For maximum efficiency the WEDG process should be used for rough machining and the truing process should be used for finish machining.

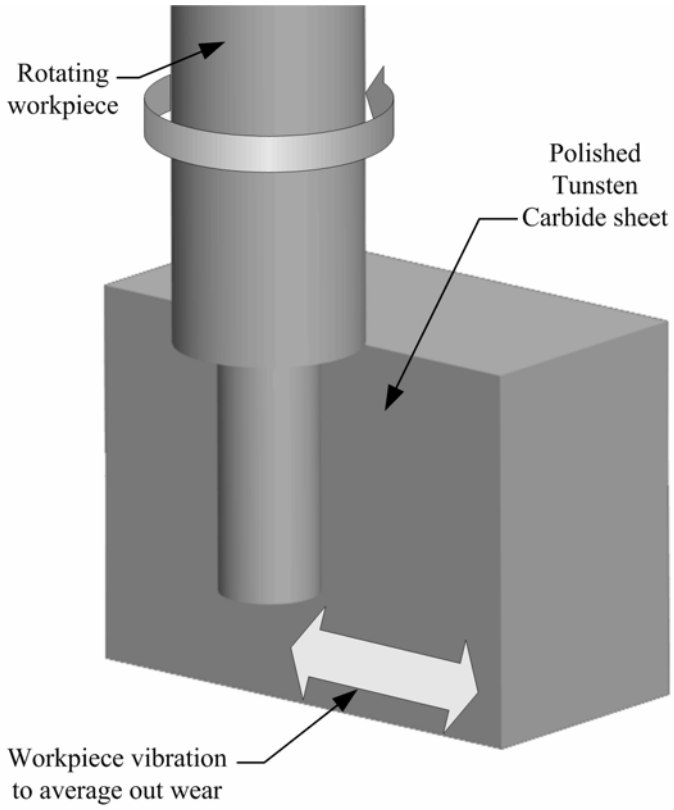

Figure 35. Diagram of cylindrical tool truing

3.4.2. Precise Cone Fabrication

Precision cone fabrication is identical to the precision cylinder fabrication except the polished tungsten carbide sheet is at an angle. The rotating workpiece approaches the sheet from the top and discharges until the edge of the cone is trued to the correct angle. Again, only a few

micrometers should be removed and the WEDG process should be used to generate the initial shape of the tool.

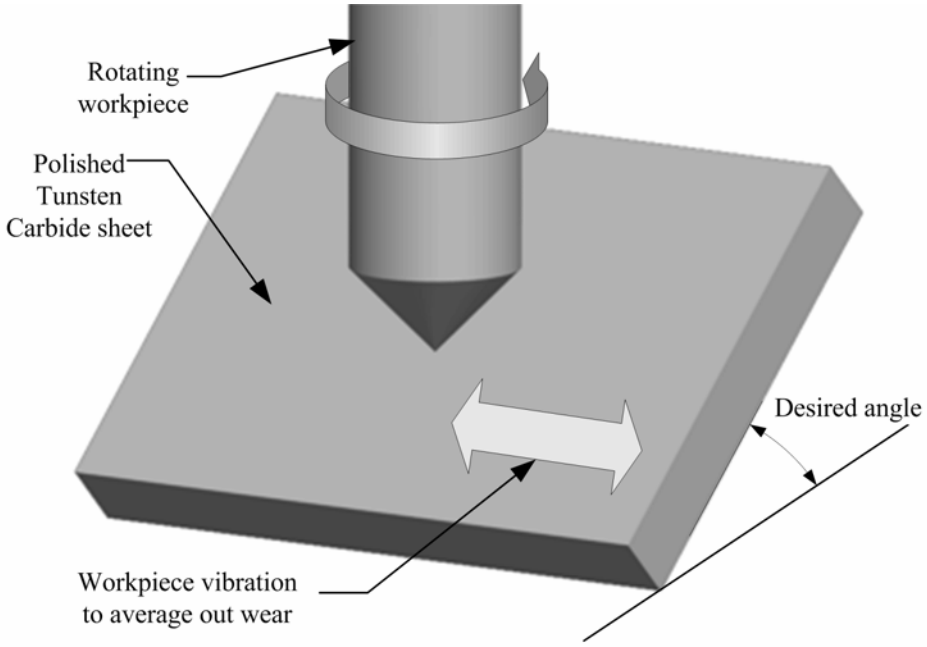

Figure 36. Conical shaped tool dressing process

3.5. Sheet Electrode Machining

In all of the previously mentioned machining operations either the workpiece or the electrode tool is rotating. Rotation creates a concentric structure and the flow of the fluid due to rotation helps flush particles away from the machining zone. If a non-concentric structure is desired two methods can be used. The first option is to machine the structure directly into the workpiece with slot or uniform wear machining. If the negative of the structure would be much easier to machine a new method dubbed "sheet electrode machining" may be used.

The first step is to machine the negative of the structure into a workpiece with a rotating concentrically shaped tool. The workpiece is aligned over the negative structure and plunged downward. The polarity of the circuit is reversed and the negative structure becomes the tool. Once the machining is completed the workpiece will have the positive structure on its surface.

The fluid around the machining zone will not flow due to the absence of rotation. To create a flushing mechanism the negative structure must be vibrated parallel to the feed direction. A vibration frequency of 100 Hz and amplitude of 10 μm is sufficient for machining structures on the order of one millimeter [31]. A piezo actuator and flexure can be used to achieve the vibration. For our experiments a Polytec PI, Inc. Nanocube is placed in the worktable reservoir and a small delrin oil reservoir is placed on the Nanocube. This prevents oil from penetrating the Nanocube and isolates the piezo from the electrical discharges. Multiple negative structures are needed due to the high wear rate during machining. For example, a shaft is needed that resembles the shape of an "H". A brass sheet is used to create eight negative structures. Figure 37 shows how the brass sheet is placed in an insulating worktank filled with dielectic oil. A tungsten wire is placed in the electrode holder and is plunged in succession over the negative "H" structures resulting in Figure 38.

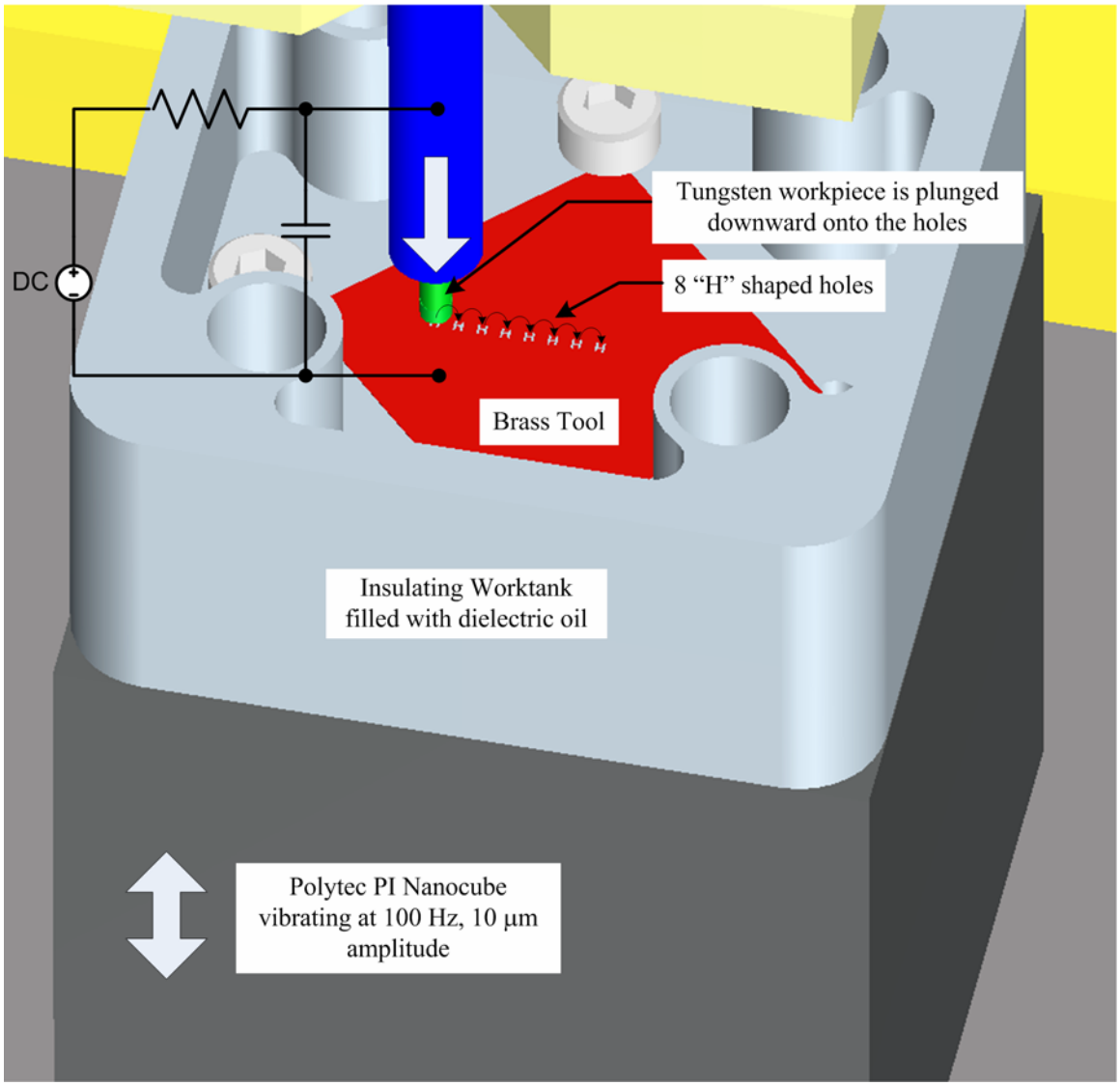

Figure 37. Sheet Electrode setup, PI Nanocube and "H" shaped brass tool.

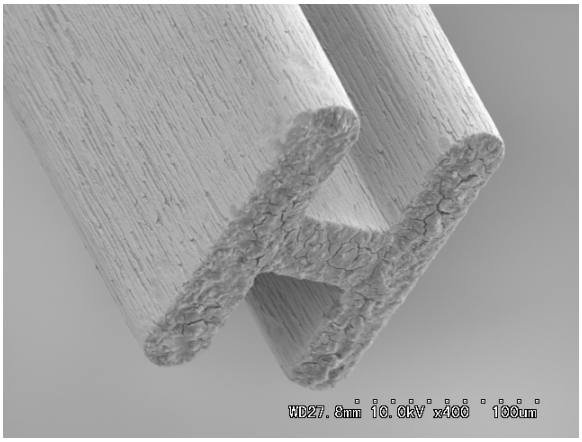

Figure 38. H-shaped electrode produced with sheet electrode process

Chapter 4. Poly Crystalline Diamond (PCD) Micro Grinding

4.1. Introduction to Chapter

This chapter describes the techniques used to achieve ductile mode grinding of brittle materials such as silicon and glass. As shown in section 1.3 polycrystalline diamond tools can be used to grind brittle materials in the ductile regime. The majority of this research has been performed on the macro-scale for fabrication of flat substrates, such as, silicon wafers and optically flat glass. The purpose of this chapter is to develop new micro grinding techniques for the realization of complex 3-dimensional microstructures in non-conductive brittle materials.

Preliminary experiments of hole and vee-groove grinding showed undesirable results. Therefore, to better understand ductile mode grinding, an experiment is designed for discovering the optimum machining parameters. Polycrystalline diamond tools like the one shown in Figure 39 are fabricated using WEDG. ULE® glass, Corning Code 7972, is chosen as the brittle material due to availability and for comparison of results obtained in other literature. Slot profiling is chosen as the machining procedure, due to the versatility in a adapting a slot to achieve more complex structures. The ability to machine all of these shapes will be important for fabricating the parts contained in Chapter 5.

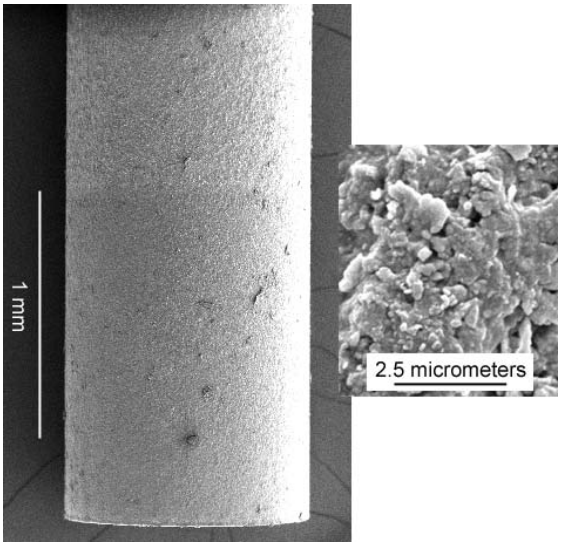

Figure 39. Poly Crystalline Diamond Tool, Cylinder and Zoomed View

4.2. Tool Fabrication

Micro electro-discharge machining is ideal for machining conductive hard materials such as tungsten carbide and polycrystalline diamond. The WEDG process can be used to fabricate simple cylindrical tools like the one shown in Figure 40. During the machining process the electrical discharges erode away the cobalt binder. The diamond particles detach and are flushed away by the dielectric fluid. Sharp diamond tips are left exposed, but binder material retains the diamonds in place. Higher discharge energy will expose more surface area of each diamond particle, but the particles will be more susceptible to dislodge from the binder material during grinding. Low discharge energy will result in a small portion of the diamond being exposed. During machining the binder material and the workpiece may come in contact, causing unwanted heat generation and brittle fracture of the workpiece.

The form of the end-face of the PCD tool is improved after WEDG by dressing with a second μEDM process that uses a polished block as the sacrificial electrode. This technique is similar to that described by Ravi et al. [32,33]. The flat polished block is oriented parallel to the PCD tool end-face, which is fed downward against the block. Flat end faces with PV values of 2 μm or less are realizable.

Both the roughness of the machined surface and the material removal rate may depend upon the roughness of the tool's cutting surfaces. Therefore, four electrodes were produced with different discharge energies by adjusting the voltage V and capacitance C during the WEDG/μEDM steps. After WEDG, the 3D surface of the four tools was measured over an area of about 288 μm × 216 μm with a commercial SWLI (Zygo NewView 5000). Form was filtered from the measured data using a high-pass filter having a cut-off wavelength of 92 μm. The results from three of the four PCD tools are shown in Figure 41. The smoothest tool was produced by the least discharge energy, and the roughness increased as the discharge energy increased. As shown in Table 3, the average roughness (R_a) for all four tools ranged between 60 and 780 nm while the peak-to-valley heights ranged between 2.10 and 8.28 μm.

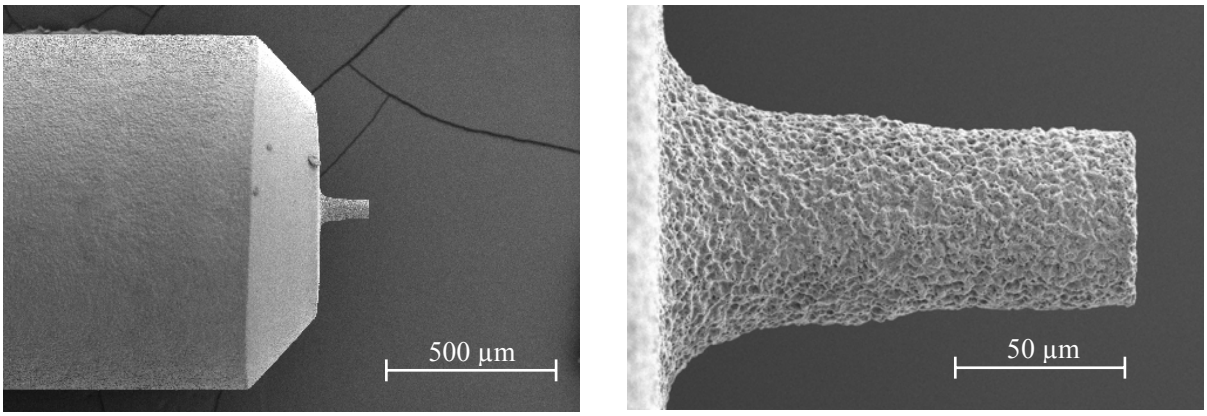

Figure 40. PCD cylindrical tool machined with WEDG

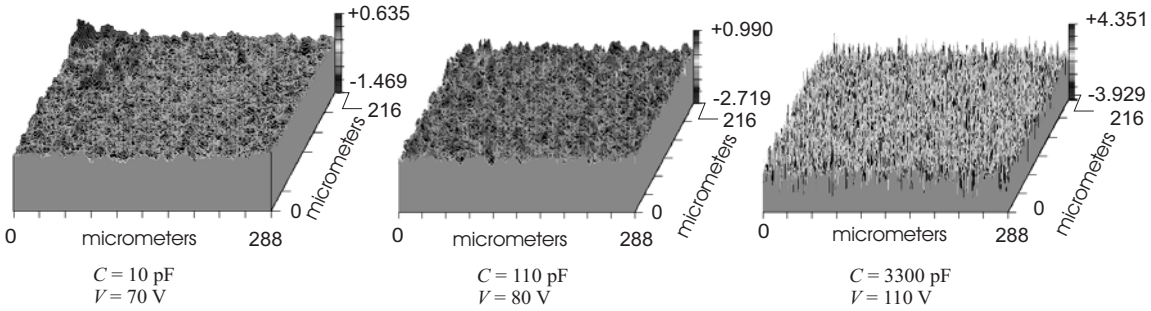

Figure 41. 3D surface heights, measured by SWLI and high-pass filtered at 92 µm

Capacitance, C (pF)	Voltage, V (V)	Energy, ½CV^2 (µJ)	Peak-to-Valley Height (µm)	Avg. Roughness, R_a (µm)
10	70	0.025	2.10	0.06
110	80	0.350	3.71	0.13
220	100	1.10	6.90	0.53
3300	110	20.0	8.28	0.78

Table 3. Peak-to-valley heights and average roughness (R_a) of PCD tools processed with increasing discharge energies during WEDG/µEDM

Higher magnifications in the Figure 42 inset show the protruding nature of the diamond grains after shaping the tool by WEDG or µEDM. Energy dispersive spectroscopy (EDS) was conducted on a machined PCD tool to determine whether the relative percentage of carbon and cobalt differed between the protruding peaks and valleys. As shown in Table 4, the surface at the peaks contain about 20% less cobalt compared to surface in the valleys, which suggests that the protrusions are mostly diamond grains. Tungsten was also present on the surface of the tools. The tungsten results when a polished tungsten carbide block is used as the sacrificial electrode and the molten tungsten particles are re-deposited on the surface of the tool.

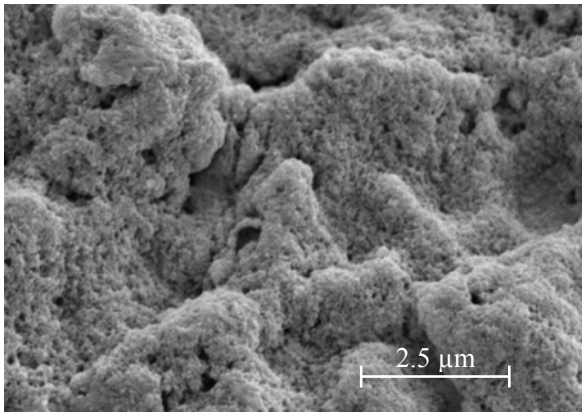

Figure 42. Zoomed View of Diamond Grain Structure

	Carbon % weight	Cobalt % weight	Tungsten % weight
Peak	83.33 +/- 0.45	6.69 +/- 0.17	9.98 +/- 0.61
Valley	61.21 +/- 0.50	26.59 +/- 0.42	12.20 +/- 1.01
Average	79.29 +/- 0.47	12.92 +/- 0.25	7.79 +/- 0.71

Table 4. Carbon and cobalt content in peaks and valleys of a PCD tool after µEDM

4.3. Preliminary Demonstrations and Observations

4.3.1. Micro Grinding of Vee-Grooves in Glass

To discover the capability of micro grinding of brittle materials, several micro geometries are attempted. The first geometry is 90º vee-shaped grooves, which are commonly used to precisely locate micro cylinders. Cone shaped tools are fabricated and used to grind the grooves in ULE glass and single crystalline quartz, see Figure 43. To determine the optimum machining conditions a series of grooves are fabricated with increasing feedspeed. The highest feedspeed at which no brittle fractures occurred was 5 µm/s. Figure 44 is a SEM image of a groove machined in the glass. This feedspeed yields a very low material removal rate. Material removal rate can be calculated from the following equation:

$$MRR = d \times 2r \times v_f \tag{4-1}$$

Where d is the cutting depth, r is the tool radius, and v_f is the feedspeed. The resulting material removal rate is very low, 25 $\mu m^3/s$. A groove 2 mm long and 80 µm deep takes approximately 24 hours to machine.

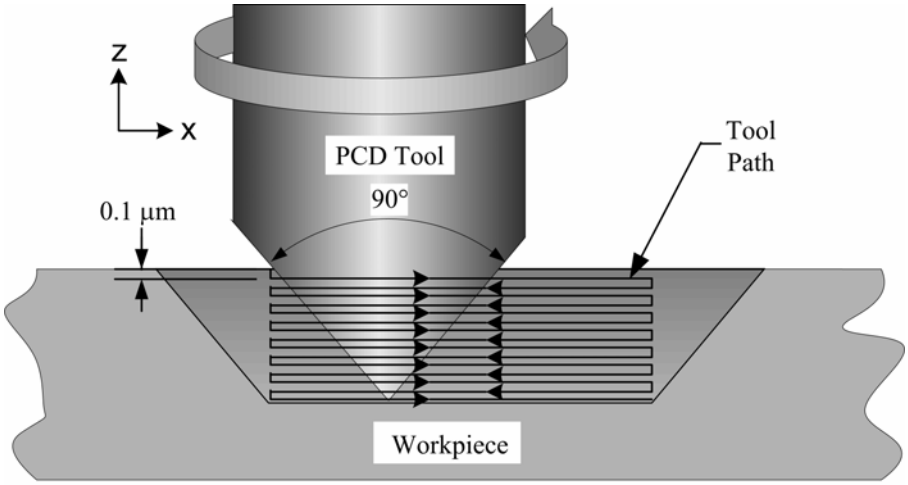

Figure 43. Diagram for grinding of vee-shaped grooves in Soda lime glass

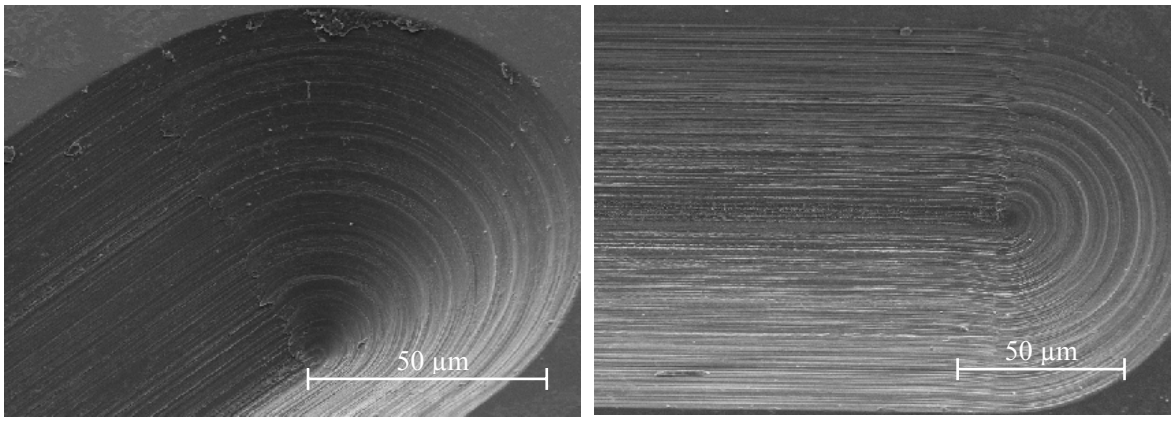

Figure 44. Vee-groove machined in Soda Lime Glass

Figure 45 is an optical microscope image of the PCD tool after machining the glass. The glass particles present on the surface could cause brittle failure when they come in contact with the glass workpiece. To eliminate this problem a pumping system is added to the micro EDM that pumps the dielectric fluid at 316 mL/min. Pumping the dielectric oil through the machining zone will flush the glass particles away from the PCD tool. The experiment was tried again and no glass particles were observed on the PCD tool, but the feed speed was only increased to 10 µm/s.

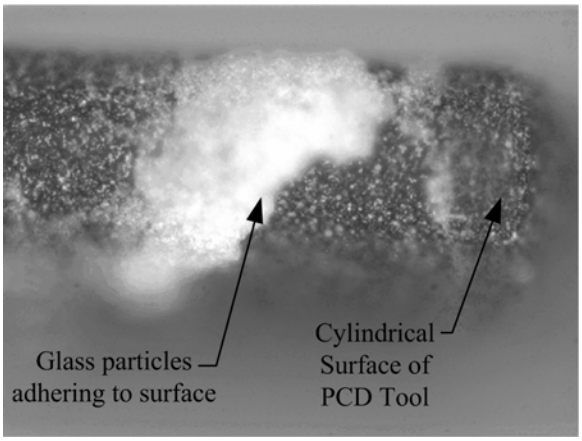

Figure 45. PCD tool after machining soda-lime glass vee-groove

The low material removal rate is due to the lack of cutting edge speed supplied by the grinding tool. On the macro-scale the tool speeds at the contact points are usually high and the pressure applied by the tool is also high, which results in a high specific energy applied to the workpiece by each diamond tool. For micro grinding the tool speeds are low due to the small tool radius. A simple solution would be increase the rpm of the tool, but this is not possible with the Panasonic MG-ED72W because problems arise from vibration and accuracy due to spindle error motion.

To improve the material removal rate a new technique is devised. The tool cutting edge speed at the center of the cone shaped PCD tool is zero and the speed increases linearly with the radius. To increase the tool speed the edge of a cylindrical PCD tool is used. The workpiece material is set at a 45º angle, see Figure 46. The results from this experiment did not yield ductile mode grinding, due to the system of grinding. The side of the groove that contacted the bottom of the tool always yielded brittle fracture, see Figure 47.

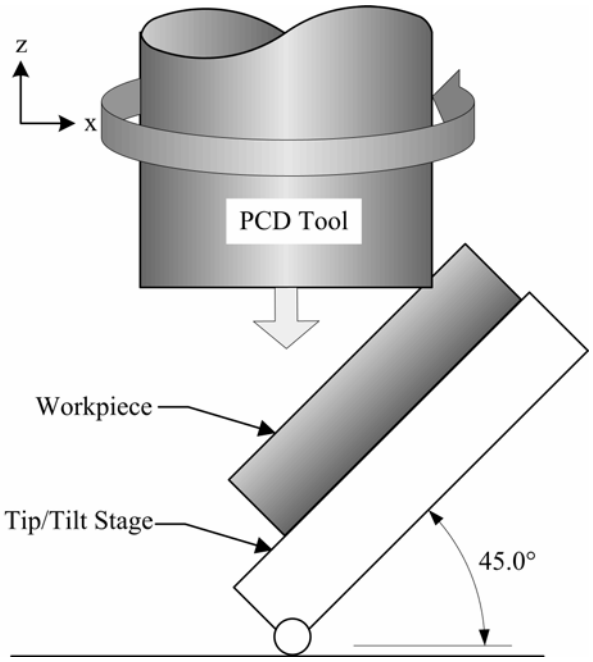

Figure 46. Diagram of PCD edge method for machining vee-shaped grooves

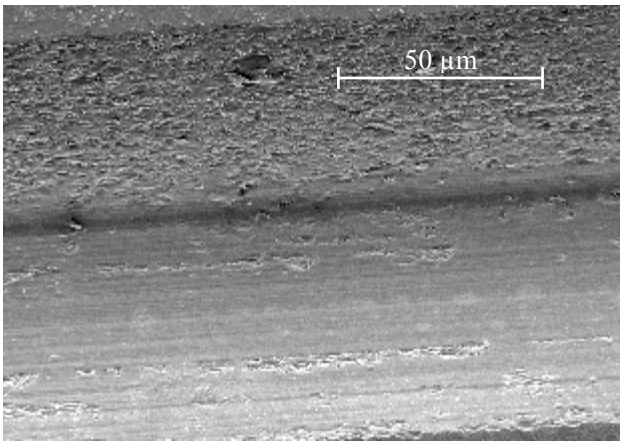

Figure 47. Single crystalline quartz machined with PCD edge method

4.3.2. Micro Grinding of Holes

Micro holes were attempted using the tools shown in Figure 48. The tool was fed straight into a soda-lime workpiece with the slowest feed rate possible on the Panasonic MG-ED72W, 0.1 µm/s. Figure 49 a) is an SEM image of the hole. Brittle fractures were observed around the edges of the hole, but the bottom hole showed ductile mode grinding. One hypothesis for the fracturing was inconsistent micro structure in the soda-lime glass therefore a hole was attempted using single crystalline quartz as the workpiece. The SEM image shown in Figure 49 b) shows

that the fracturing around the edges was reduced but small brittle fractures were observed over the entire hole. The single crystal quartz appears to "flake" when ground with a PCD tool.

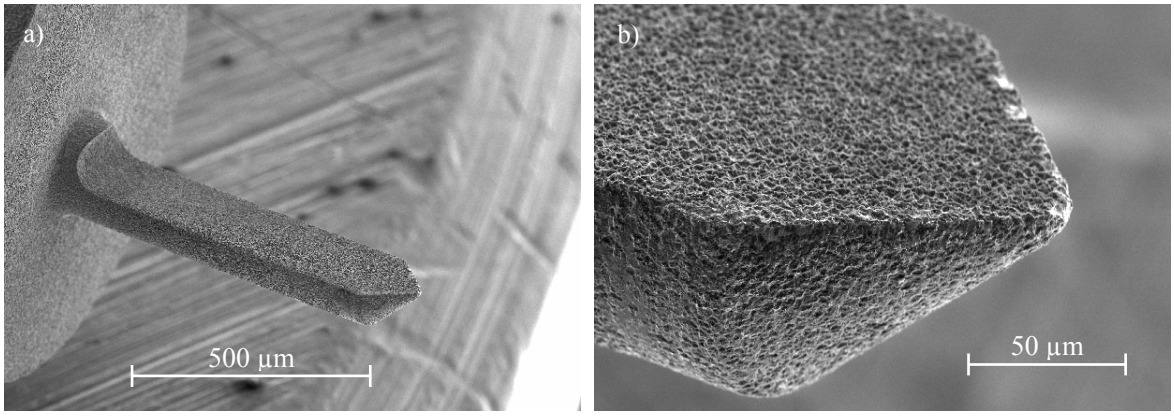

Figure 48 a) PCD tool for drilling holes in brittle materials b) zoomed image of the cutting edge

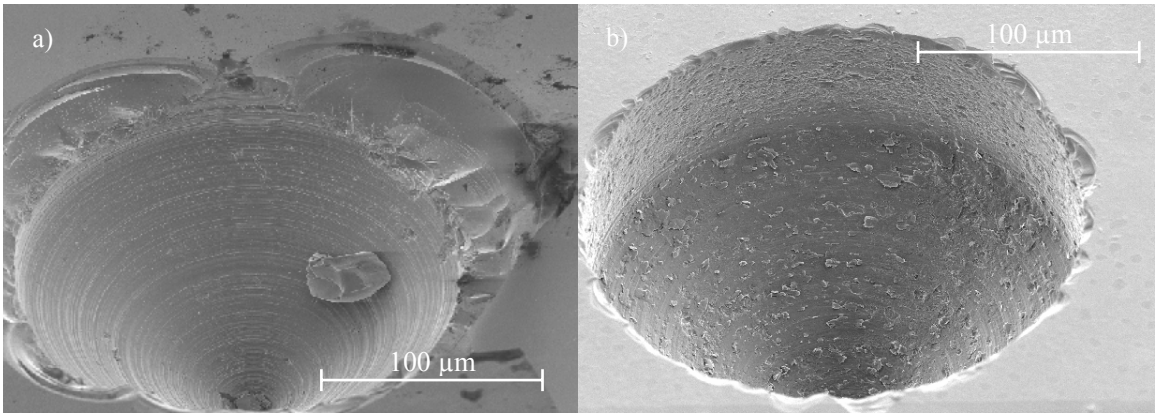

Figure 49 a) Hole drilled in Soda Lime Glass b) Hole Drilled in Single Crystalline Quartz

4.3.3. Summary of Preliminary Demonstrations and Observations

The mechanisms and details of the grinding process clearly are not understood and must be investigated. The remainder of this chapter is devoted to discovering the mechanisms involved during ductile mode grinding of complex microstructures. Once these mechanisms are understood the tool path and grinding procedure can be altered to achieve ductile mode grinding with higher material removal rates.

4.4. Experimental Measurement of Grinding Forces

4.4.1. Analytical Model

From equation (1-3) the specific energy during the grinding process is a function of the cutting force and the cross sectional area. Therefore, because the specific energy is constant the cutting force during ductile mode grinding is constant, regardless of the feed speed. Preliminary experiments of micro grinding of brittle materials have shown that the statement above does not hold true. If the cutting depth is held constant and feed speed is slowly increased, brittle fracture eventually occurs. To investigate why, the uncut chip area is analyzed. The micro milling process is similar to fly cutting on the macro scale with a carbide insert fly cutting tool. If the bottom of the diamond particles is treated as flat, the uncut chip area (A) for a milling operation can be written as:

$$A = \frac{30 \times \alpha \times v_w \times d}{\pi \times \omega} \qquad 2$$

where d is the depth of cut into the workpiece, ω is the spindle rpm, α is the radians between cutting edges (or inserts in the flycutting analogy, and v_w is the workpiece feed, see Figure 50. As can be seen from equation 2 the uncut chip area can be minimized by decreasing the distance between the cutting edges, the feed speed, and the depth of cut. The uncut chip area can also be reduced by increasing the spindle rpm.

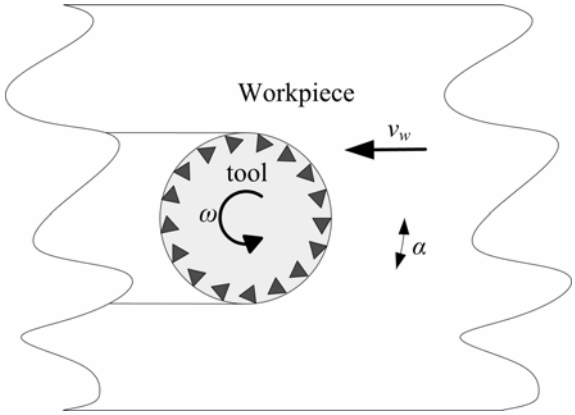

Figure 50. Diagram of velocity vectors for milling operation

Chip extraction must also be considered for ductile mode grinding. If the chips are not immediately flushed away and no gap exists between the cutting edges, then the chips adhere to

the tool surface. Glass chips colliding with the glass workpiece is not ideal and can cause brittle fracture. Increasing the feed speed produces a larger un-cut chip area, therefore, creating larger chips. Truing the tool to a smaller R_a value will reduce α which will reduce the gap between the cutting edges. A hypothesis is extracted from this argument; high feed speed and low tool R_a can cause a different mode of brittle fracture than the one discussed by Bifano.

4.4.2. Experimental Design

To test the hypothesis presented in the previous section, an experiment is designed. The parameters of the experiment are summarized in Table 5. The tool, workpiece, and tool path are shown in Figure 51. The RPM and cutting depth are held constant to limit the scope of the experiment. A Panasonic MG-ED72W μEDM machine with three axis capability will be used for the tool positioning. A total of four grooves 250 μm long and 5 μm deep are machined in Corning ULE® glass with feedspeeds of 1, 2, 3 and 4 μm/s. These feed speeds are chosen based on preliminary demonstrations (Section 4.3.1) conducted in ULE glass. Fifty nanometers is the smallest step size for the μEDM machine; therefore, the plunge depth is set to this value. This value is approximately one order of magnitude below the tool R_a value therefore cutting should occur at the sharp tip of the grains and the chips should not clog the interstices of the tool. The same tool is used for all 4 grooves and the tool is not re-trued between each groove.

Parameter name	Parameter value
PCD tool	Sumitomo Electric ~0.3 micron grain size
Workpiece material	ULE® glass, Corning Code 7972
RPM	3000
cutting depth	50 nm
feedspeed	1,2,3 and 4 μm/s

Table 5. Experiment parameters for grinding of ULE glass

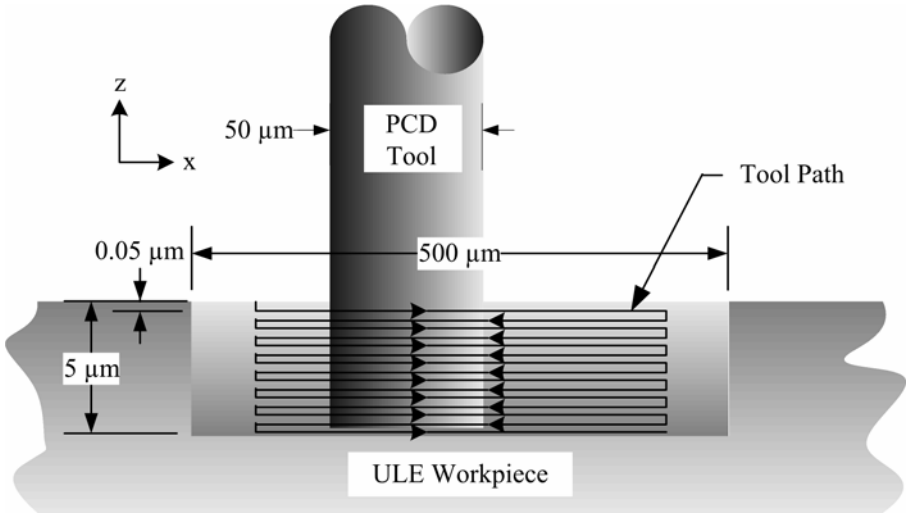

Figure 51. Tool path for PCD profiling of ULE glass

4.4.3. Tool and Workpiece Characterization

The end milling tool shown in Figure 40 was used for this experiment. The details of elemental composition are included in section 4.2. A zygo 3-D surface scan of the end-face of the tool is shown in Figure 52. The R_a value is 0.536 micrometers and the PV value is 3.14 micrometers. This indicates that the tool is rough but flat. The high roughness will amplify the tool wear and simplify the analysis.

A piece of the ULE® glass is tested with a Digital Microhardness Tester, FM-7, Future-Tech Corp. The Vickers hardness is tested at 5 random with a 200 gram force applied for 10 seconds. The results listed in Table 6 show that ULE glass has an average Vickers hardness of 674.34.

Vickers Hardness of ULE glass					
Test #1	Test #2	Test #3	Test #4	Test #5	Average
716.5	638.5	605.4	704.1	707.2	674.34

Table 6. Vickers Hardness of ULE® glass

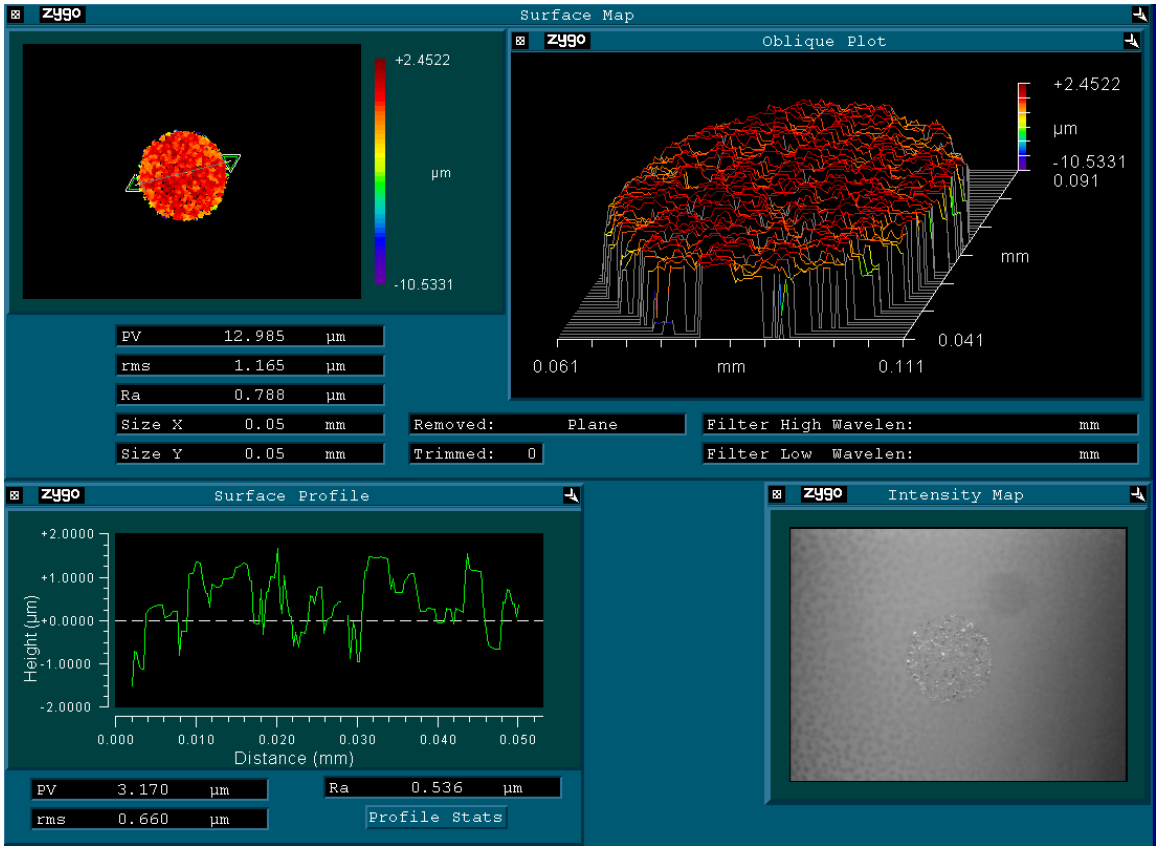

Figure 52. 3D surface scan of the PCD tool end-face electro-discharge machined with 110 Volts and 3300 pF capacitor

4.4.4. Tool Wear Analysis

After each groove was machined the tool end-face was re-measured, see Figure 54. A mask like the one shown in Figure 53 was applied to each measurement to ensure that the data taken was from the end face and not the side of the tool. The peak-valley (PV) value of the end face was measured with no filtering. The 3D measurements show that the edges of the diamond are dulling and the end-face is getting smoother. The tool experienced significant "break-in" during the first groove and the PV value remained constant at around 7 micrometers until the final groove when the PV value dropped to 4.2 micrometers.

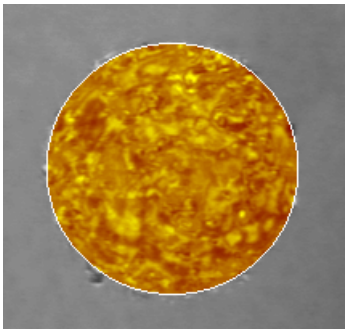

Figure 53. Mask applied to 3D scanning white light interferometer measurement of the end face of the PCD tools

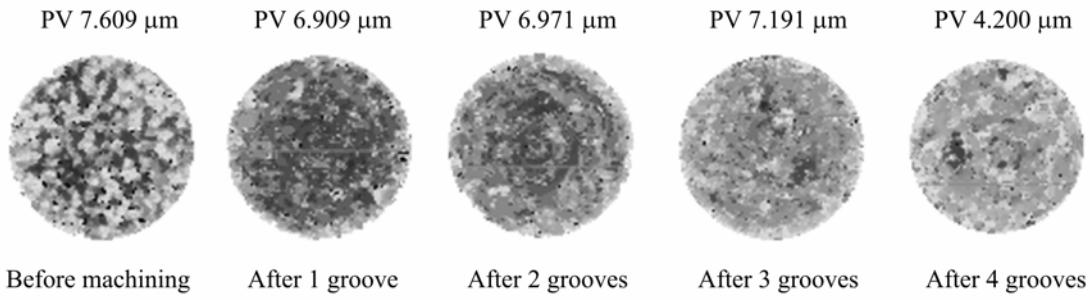

Figure 54. Form of circular end of PCD tool after cutting 4 successive pockets in ULE glass; typical peak (red) to valley (blue) height is about 2 micrometers

4.4.5. ULE Groove Analysis

SEM images of the four grooves are shown in Figure 55. Also shown are 3-D surface scans captured using a Zygo New View scanning white light interferometer. To discover the roughness on the bottom of the groove, the image was cropped and the data was filtered with a high pass filter with a 10 micrometer cutoff wavelength, see Figure 56 for an example. The R_a values are included as insets in Figure 55 and all exhibit a value on the order of 10 nanometers, which suggests little dependence on feed rate.

Observation of the SEM and zygo images shows that all of the grooves display ductile mode grinding and can be considered "good" except Figure 55 d) which has considerable fracture and chip breakout around the edges. These fractures result from high cutting forces in the horizontal plane causing crack propagation and sub-surface damage to the point that glass chips break away from the edges. Two factors can cause increased forces in the horizontal plane,

increased feed speed and tool wear. For this experiment the feed speed is, of course, increased and tool wear is exhibited, see Figure 54.

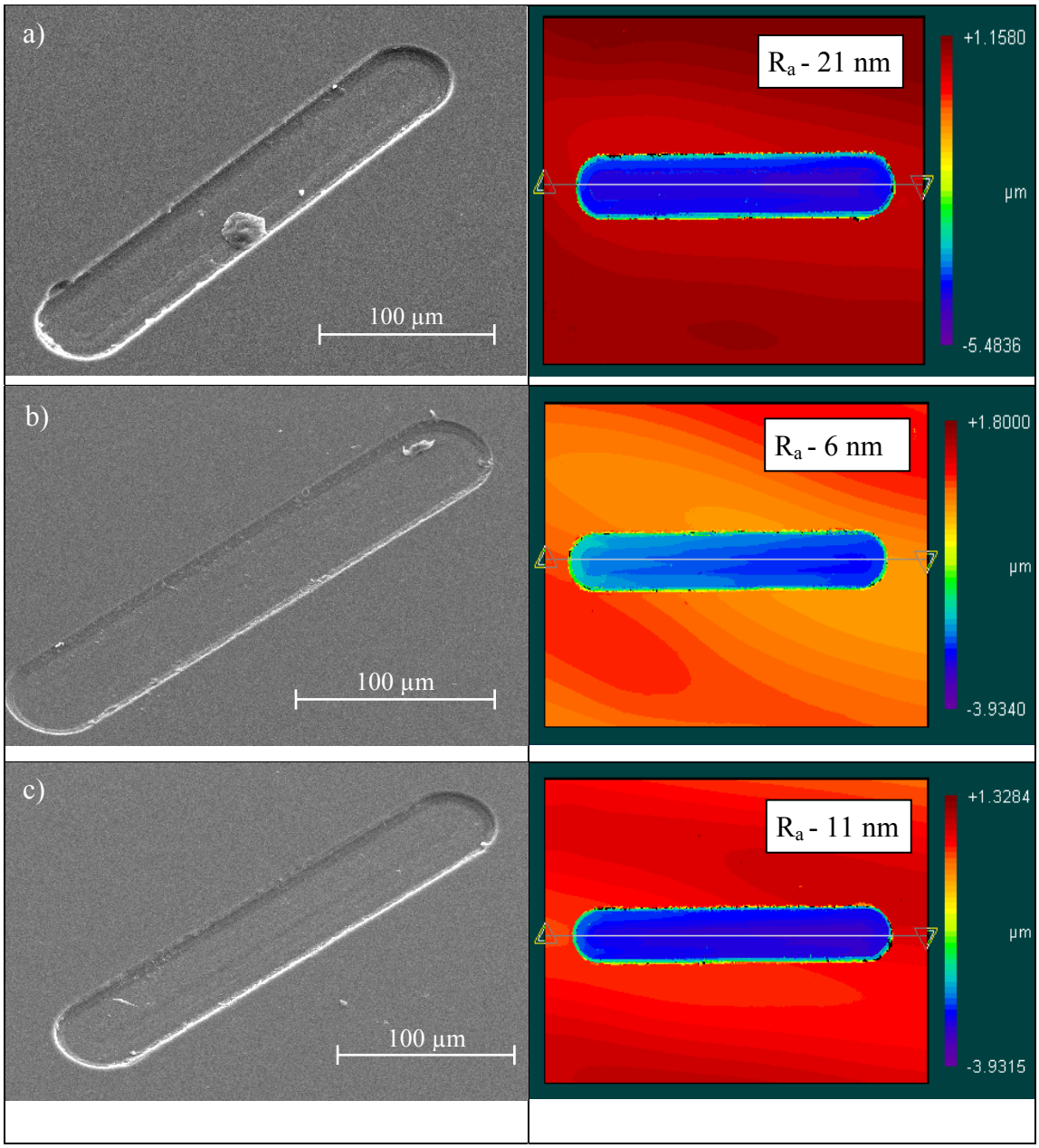

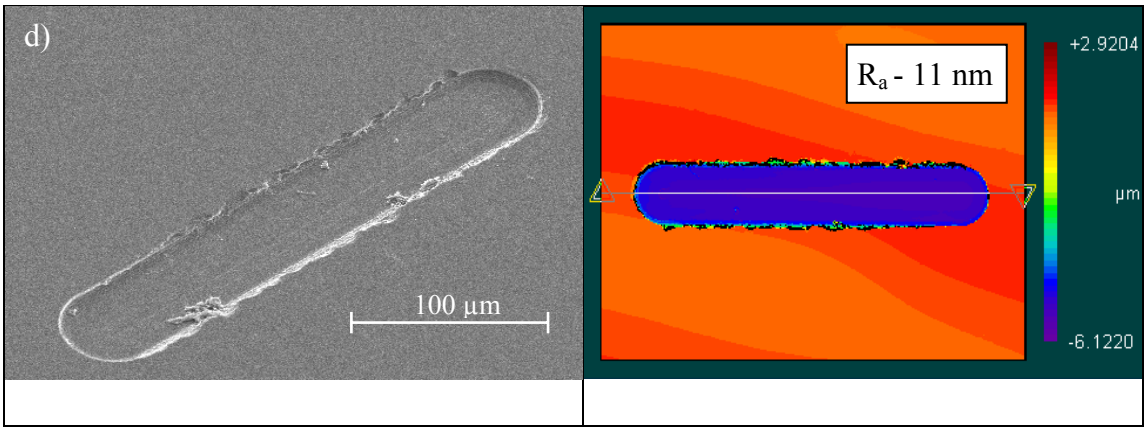

Figure 55. Grooves in ULE glass, feed speed a) 1 µm/s b) 2 µm/s c) 3 µm/s d) 4 µm/s

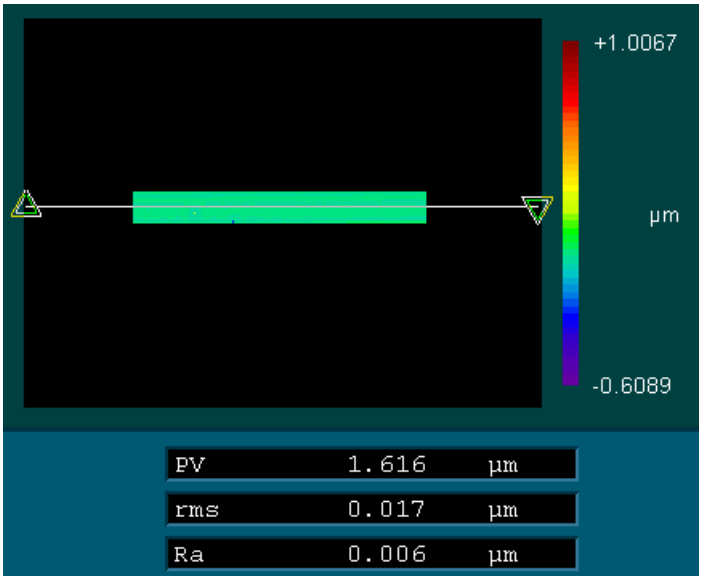

Figure 56. Zygo 3D surface scan of ULE groove #2 masked and filtered to discover the roughness on the bottom of the groove

4.4.6. Cutting Force Analysis

The ULE glass was placed in a worktank which was mounted to Kistler Minidyne Dynamometer as shown in Figure 57. The PCD tool was mounted in the micro EDM spindle which rotates at 3000 rpm. Figure 58 shows how the glass workpiece is placed in a tank which funnels the dielectric oil down away from the dynamometer to prevent contamination.

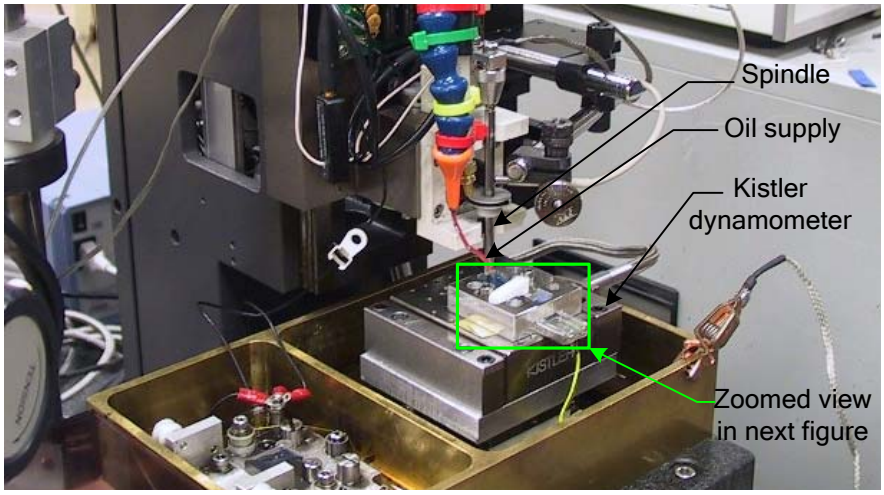

Figure 57. Experimental setup displaying the spindle and dynamometer

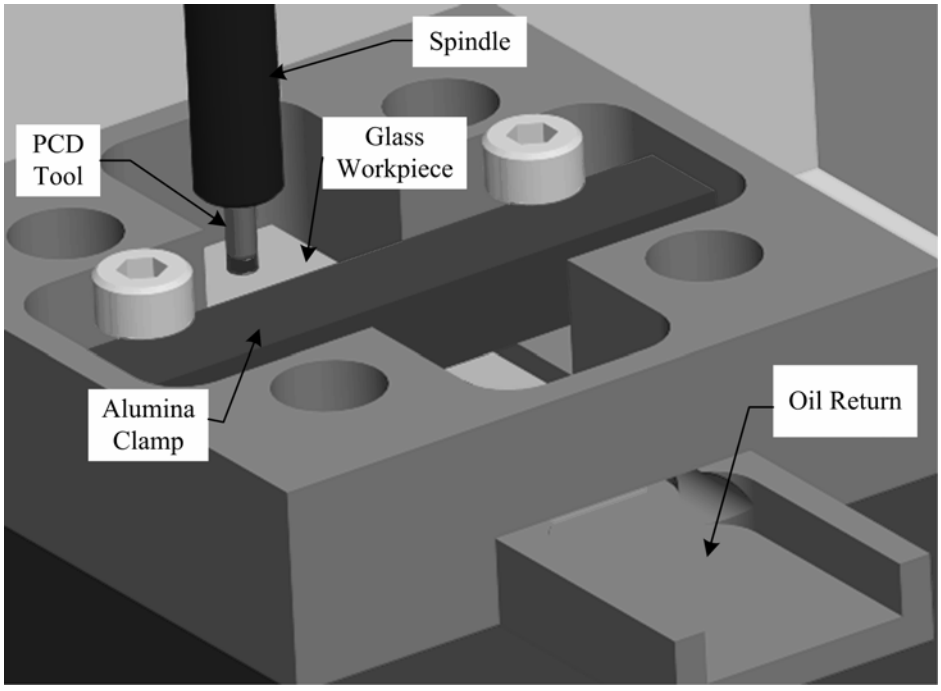

Figure 58. Zoomed view of the experimental setup displaying workpiece and tool.

The cutting forces were sampled at 5 kHz in 20 second segments for the entire machining process. Each 20 second segment was fit to a tenth order polynomial and each force data point was subtracted from the polynomial to eliminate the thermal drift in the force sensors. The root mean square value of each 20 second segment was taken from the filtered force data and recorded in a new matrix. The resulting off-axis, feed axis, and plunge axis cutting forces are plotted in Figure 59, Figure 60, and Figure 61 respectively.

As can be seen from the figures, the cutting forces in the feed and off-axis directions are relatively low and stable at the beginning and become higher and more unstable as the length of tool engagement increases. This can result from two phenomenon; higher forces on the wall of the groove due to reduced chip extraction, and new cutting edges on the side of the tool due to straightness errors in the fabrication of the tool. The plunge axis cutting force is an order of magnitude above the other cutting directions indicating that the cutting edges are at the bottom of the tool and not the side.

Groove 2 experienced the lowest plunge axis cutting forces and the lowest cutting forces overall. Groove 2 also had the lowest R_a value, indicating that machining conditions were optimal for this groove. Groove 1 experienced erratic and high cutting forces during machining, which is counterintuitive considering the tool was not worn during this groove. The tool experienced significant "break in" during the machining of the first groove which indicates that the tool was too rough. The tool should be trued to a R_a value closer to the value before machining groove 2, which was 0.415 μm.

During the machining of the fourth and final groove the off-axis forces experienced a significant jump. This jump could be due to the fact that the tool was worn significantly causing the swarf to become trapped on the side walls of the tool. These trapped particles then cut into the side of the groove causing the sides to fracture out. This phenomenon was discussed earlier. These results indicate that a tool should be re-trued between each groove to maintain adequate interstices between the diamond grains to allow chips to accumulate.

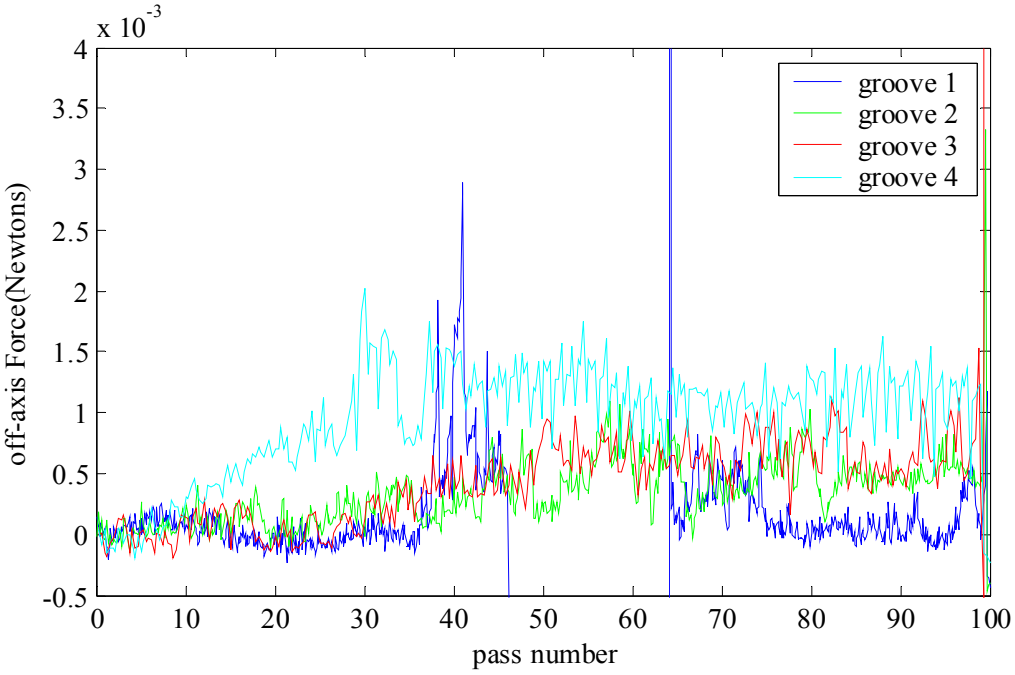

Figure 59. Off-axis cutting force measurements during grinding of ULE glass

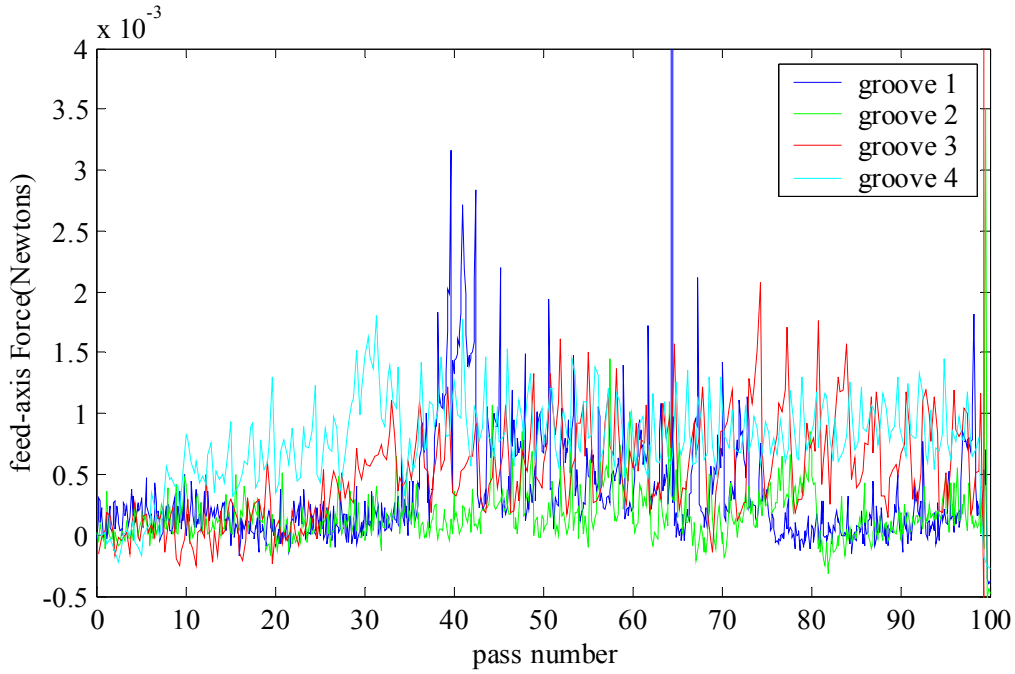

Figure 60. Feed axis cutting force measurements during grinding of ULE glass

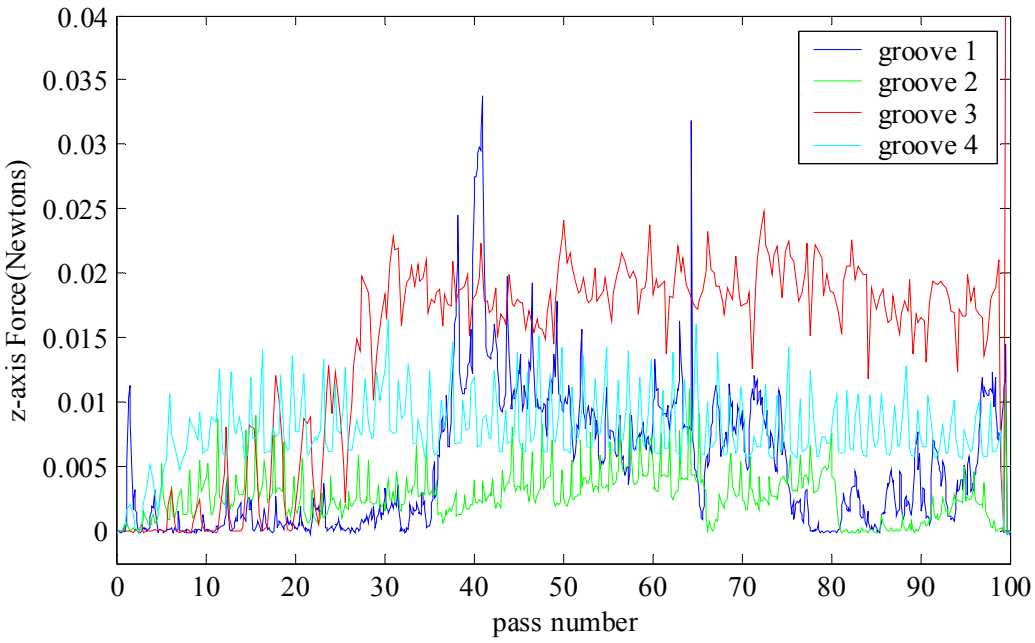

Figure 61. Plunge axis cutting force measured during grinding of ULE glass

4.5. Chapter Summary

The results above show that ductile regime grinding did occur with sharp tools and slow feed speeds. Once the tool is dulled and feed speed is increased brittle fracture is observed. Analysis of the cutting forces revealed the cutting edge is at the bottom of the tool and not the side. The results above prove the hypothesis discussed earlier that the uncut chip area can be reduced, but only to a certain point before the chips begin to clog the tool. When the tool is sharp and feed speeds are slow surface finishes down to 6 nanometers are realized.

The material removal rates during ductile grinding are very low which can restrict applications in real world products. But, with the knowledge gained from this experiment, further experiments can be conducted to increase the material removal rate and improve process quality and reliability. Some potential improvements are increased rpm, ultrasonic vibration assistance, in process tool dressing, and improved flushing techniques.

Chapter 5. Applications for Micro EDM

5.1. Micro Flexure

Martin Culpepper, Assistant Professor of Mechanical Engineering at MIT, is developing the HexFlex flexure technology. These monolithic compliant mechanisms allow for precision movement and alignment on the order of a nanometer. Figure 62 is a micro HexFlex mechanism designed at MIT. This HexFlex is machined from a 100 μm thick stainless steel sheet. If the tabs are displaced in the x and y direction, see Figure 63, the center platform will displace and/or rotate due to the low stiffness of the thin beams connecting the tabs. Combinations of displacements on the three tabs will yield unique displacements and rotations at the center. Therefore, this flexure has 2.5 degrees of freedom.

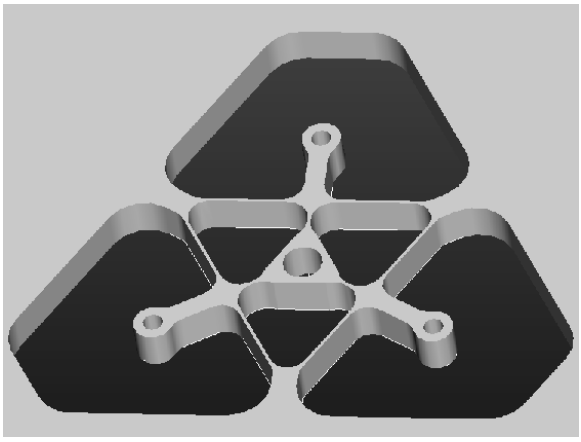

Figure 62. Hex Flex, micro flexure

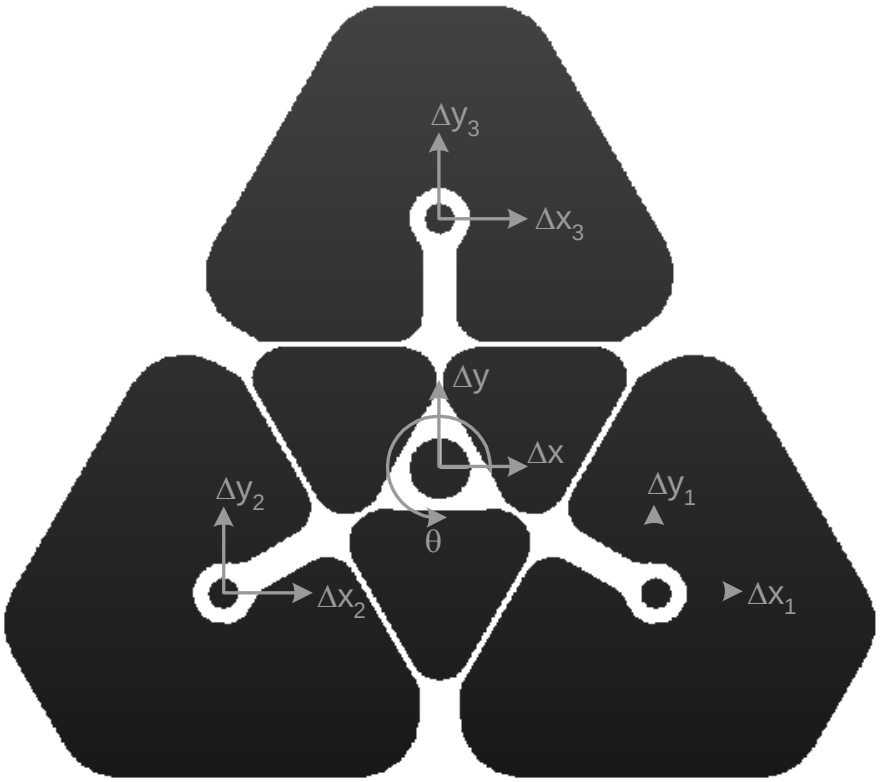

Figure 63. Diagram of 2.5 axis micro flexure stage

To achieve this complex shape, the uniform wear method of machining is chosen. Tool paths must be created that overlap and will be simple to program. Due to the sharp radius, a two-step process is chosen. First a large electrode will remove the bulk of the material, and in the second process a small electrode will trace around the edges to produce the thin beams. Figure 64 is a diagram of the tool paths selected for the two tools. For the large diameter tool the path creates a closed loop, therefore the direction after each loop the direction is reversed. For the small diameter tool, an open path achieves the outside of the beams. At the end of each path the tool steps down at that point and traces back to the beginning of path. These methods prevent uneven wear along the path. Attempts at machining the micro HexFlex have been unsuccessful so far, but this is due to machine malfunctions due the long machining time of this complex part. Figure 65 is Hexflex machined only 20 μm deep, but the tool paths generate the desired structure.

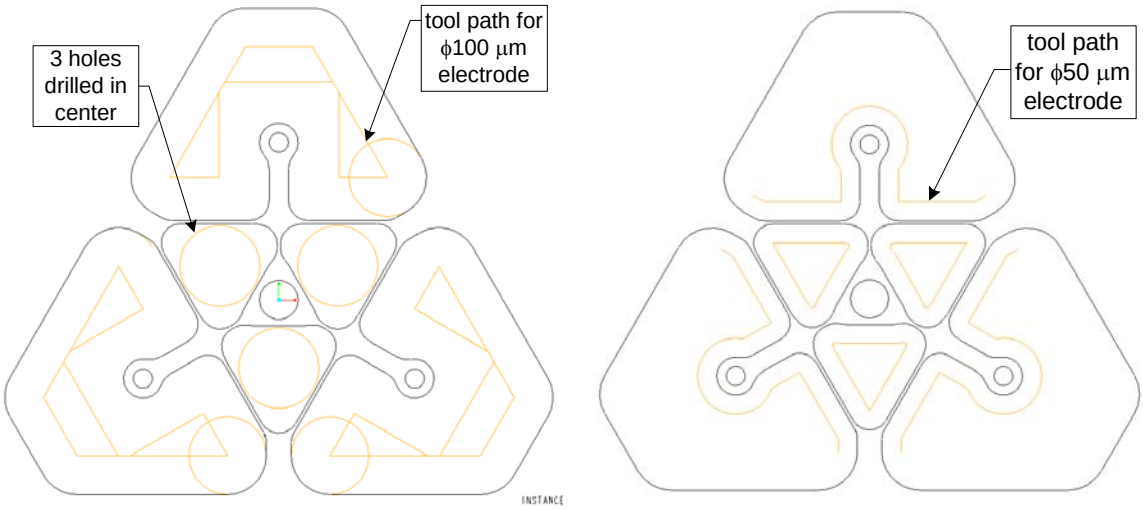

Figure 64. Tool paths for achieve the micro HexFlex

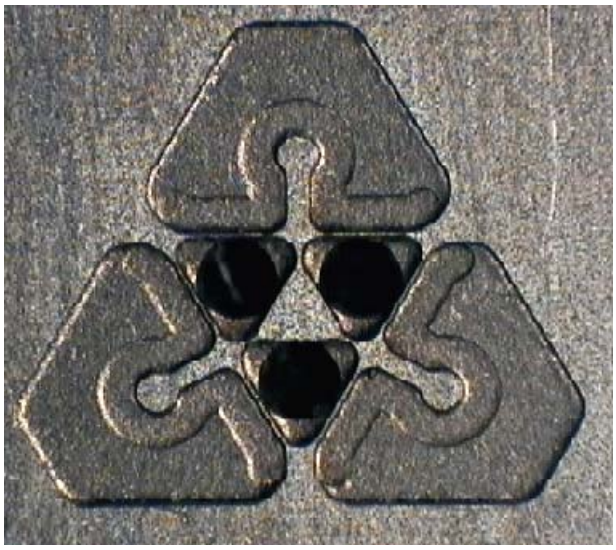

Figure 65. Micro HexFlex partially machined

5.2. Optical Waveguide

For fiber optic connectors an optical fiber is placed inside the male or female end of the connector, called the ferrule. When the male and female ferrules are connected, the ends of the optical fibers should line up exactly to transmit the waves. Tolerances on the order of 0.5 μm are commonly desired to achieve 100% light transmission. To achieve these tight tolerances

precision vee-grooves are fabricated in the ferrule. The optical fibers are then placed into the grooves and the connector is assembled around the fibers. If the male and female connectors have identical vee-groove locations, the fibers will line up.

Fabrication of the vee-grooves is a critical step in the process. A mold or tool is fabricated upon which all of the parts are based. Some manufactures make a mold for injection molding and others make a lapping tool. The lapping tool is an inverse of the desired shape and is made of a harder material than the final part. Teradyne, Inc. used a lapping tool for their connector, but the part tolerances were out of spec. They used a wire electro-discharge machine to fabricate the lapping tool out of tungsten carbide. To improve the tolerances, the vee-grooves in the lapping tool were ground with a PCD cone shaped tool. Figure 66 is an SEM image of the lapping tool. The PCD cone tool was used to machine ten micrometers of material from the center vee-groove, and the groove to the right is the original surface machined with wire EDM. The surface finish and the form of the tool have been improved. The discolorations seen in the bottom of the groove were not surface defects, but rather binder material propagating to the surface. Figure 66 b) shows that the cutting lines are continuous across the discoloration therefore this is not a defect.

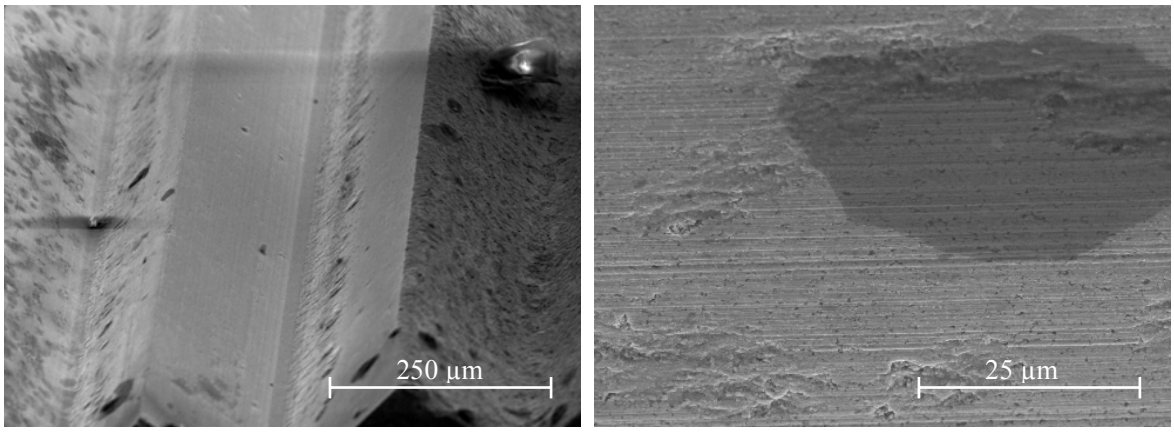

Figure 66. a) Vee-groove machined in Tungsten Carbide and zoomed view of the surface b) zoomed image of the surface

5.3. Platform for Carbon Nanotube Probe

A new technology developed at the University of Kentucky allows carbon nanotubes to be used for machining on the nano-scale. The main obstacle in the realization of this technology is the placement of a single carbon nanotube in a desired orientation and position. One proposed solution to this problem was to synthesize a single carbon nanotube on the tip of an Atomic Force Measurement (AFM) probe. AFM probes are typically etched in silicon like the AFM probe shown in Figure 68. A typical diameter for a carbon nanotube is 50 nm, but the radius on the end of an AFM probe is on the order of a nanometer. To create a plateau that will propagate the growth of the nanotube on the tip, the AFM probe is machined. Since the probe is on a cantilevered micro beam, the cutting forces could potentially break the beam. Therefore, UV curable epoxy is applied to the top of the AFM probe and supports the beam during machining. After machining the epoxy is washed away with acetone. See Figure 67 for the machining procedure. The first step is to discharge off the flat surface to zero the z-axis. Next, the tool is positioned over the end of the probe a lowered slowly onto the tip.

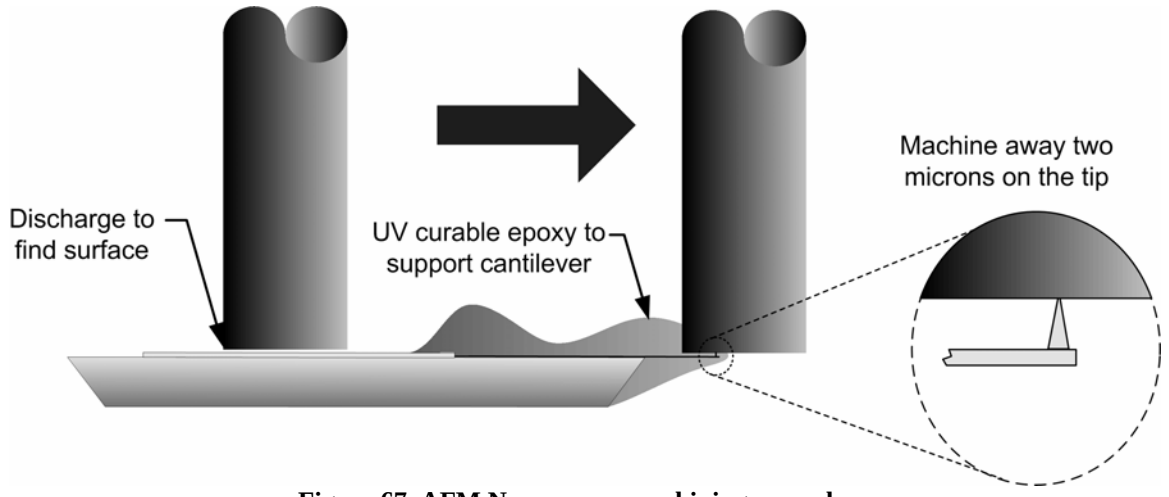

Figure 67. AFM Nanosensor machining procedure

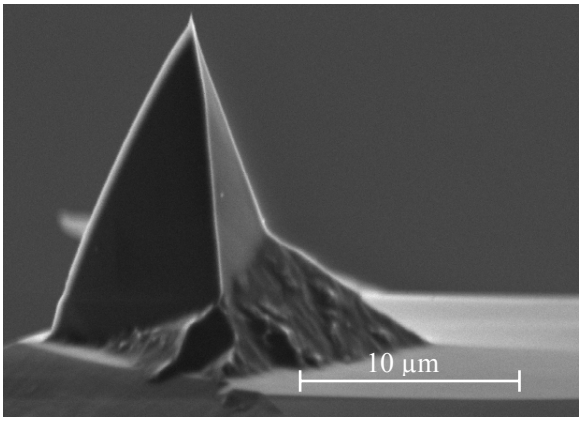

Figure 68. AFM probe tip before machining

Figure 69 contains SEM images of machined probes. As can be seen the tips contain a flat spot on the tip of the probes which almost appears to be mashed or rubbed with the tool. This process contains many inefficiencies and difficulties stemming from the inaccuracy of the micro EDM and the removal process for the curable epoxy. Approximately 1 in 20 probes were successfully machined, but the machined area varied drastically. Due to these problems other techniques not involving micro EDM are being explored.

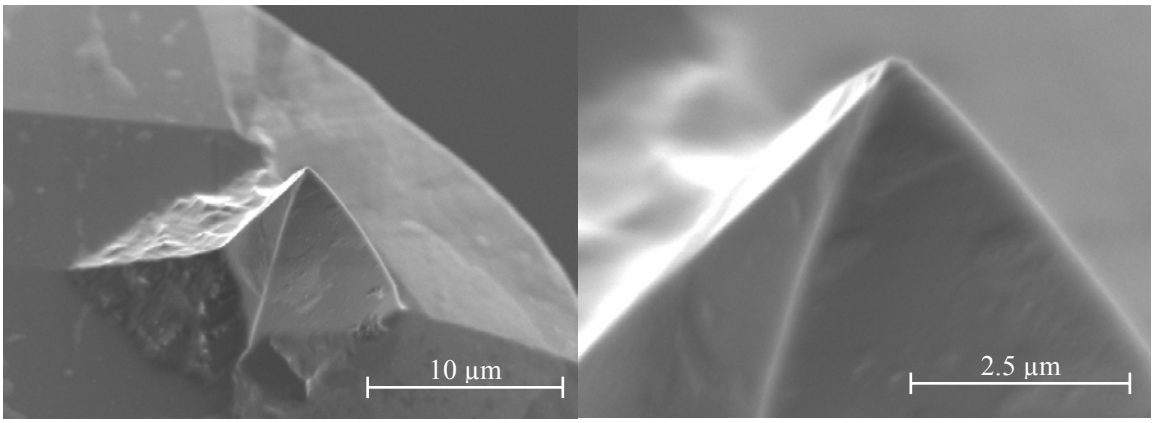

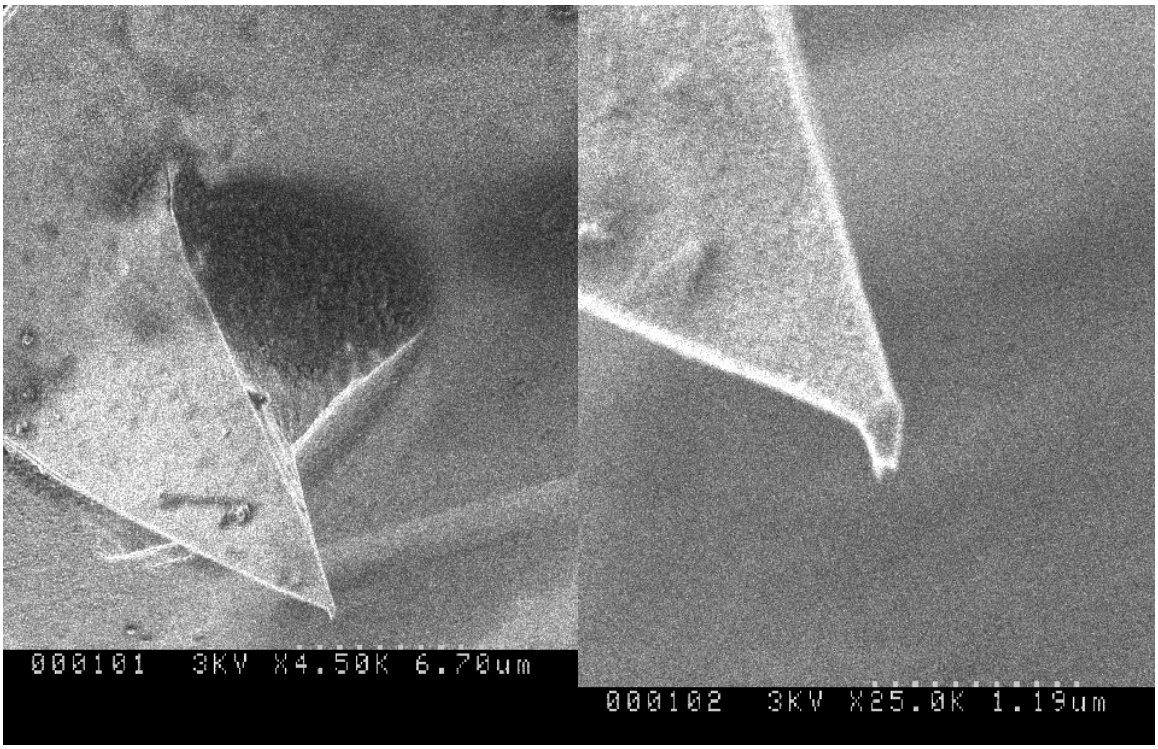

Figure 69. AFM Probe tips after machining, normal and zoomed view

5.4. Vee-Grooves in Soda-Lime Glass for Non-Conductive Precision Alignment

The test fixture for the nano machining technique described in the previous section is shown in Figure 70. To electrically isolate the cathode from the anode precision vee-grooves are fabricated in quartz. These vee-grooves precisely align the carbon nanotube with the optical fiber substrate. Using the vee-groove grinding technique, the precision vee-grooves are fabricated from Soda Lime glass. The resulting vee-grooves are shown in Figure 71. Some brittle fracture occurred at the bottom of the grooves, but the cylinders which rest in the grooves will not come in contact with this area. Placement of the pieces into the system showed successful alignment, see Figure 72.

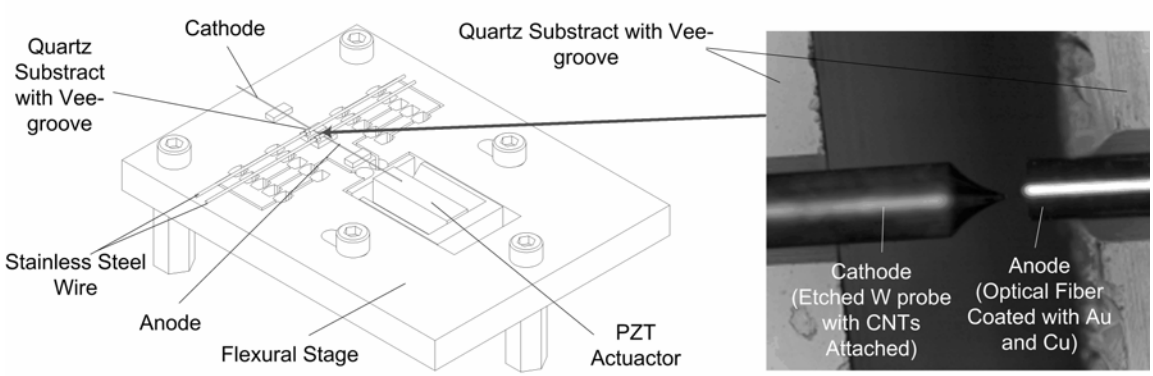

Figure 70. Test fixture for nanomachining using carbon nanotubes

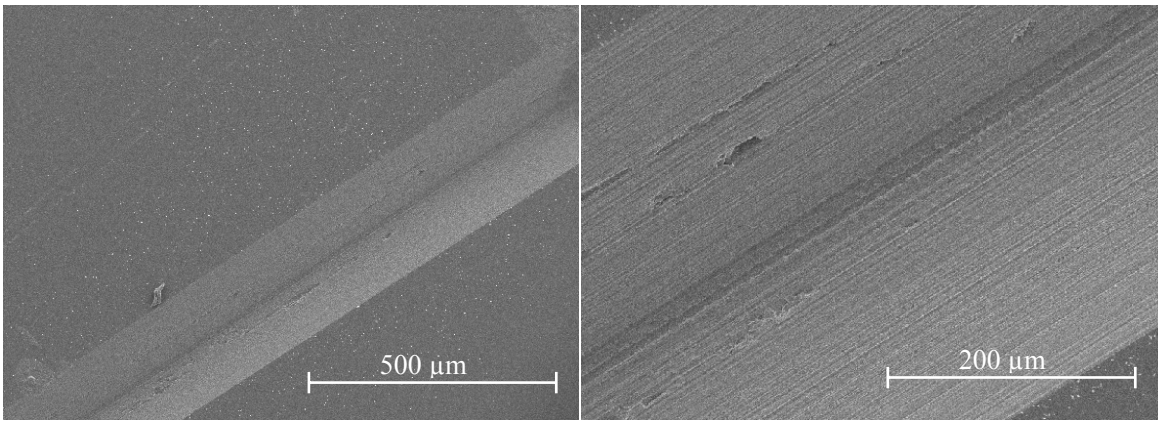

Figure 71. Vee-groove in Soda Lime glass for alignment, normal and zoomed view

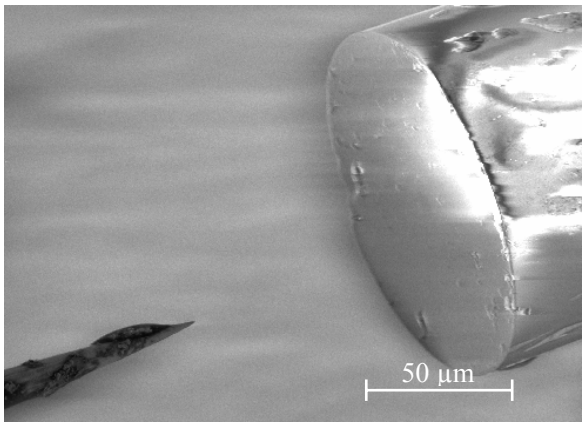

Figure 72. Nanoprobe aligned with optical fiber

Chapter 6. Conclusions and Future Work

6.1. Conclusions

The previous chapters describe the processes used to achieve complex microstructures with micro electro-discharge machining. Characterization of limitations is important to understand where micro EDM fits into the micro-manufacturing landscape. Once these boundaries are established and techniques are understood, design for manufacturing concepts can be used to develop low-cost components for industrial applications. This thesis is the groundwork for that understanding and Chapter 5 contains specific applications to these micro EDM techniques. With comprehensive knowledge of the processes described in this thesis anyone should be able to reproduce the results and have new ideas for new parts and techniques for micro EDM.

6.2. Future Work

The main goal of future work will be to improve the deficiencies of the machine discovered through empirical data obtained from this thesis work. The two main topics are; improving the straightness and surface roughness of micro-shafts machined with WEDG, and improving the material removal rate during micro grinding of brittle materials. Once these obstacles are overcome precise cylindrical PCD tools can be used to grind precise defect free microstructures in brittle materials. Several new concepts for micro components are discussed in the following sections.

6.2.1. Micro Air Bearings

Precision air bearings like the one shown in Figure 73 use a thin film of air lubrication to suspend a shaft in a housing. The airflow provides low friction, zero wear, high radial and axial stiffness, and low radial and axial error motions. These spindles have found many applications, such as, computer disks, roundness and flatness testing, and precision machining [1]. But, due to the weight and dimension of this spindle applications are limited to the macro scale. The

objective of this research is to design a micro air-bearing spindle using the design concepts applied to the macro air bearing spindle.

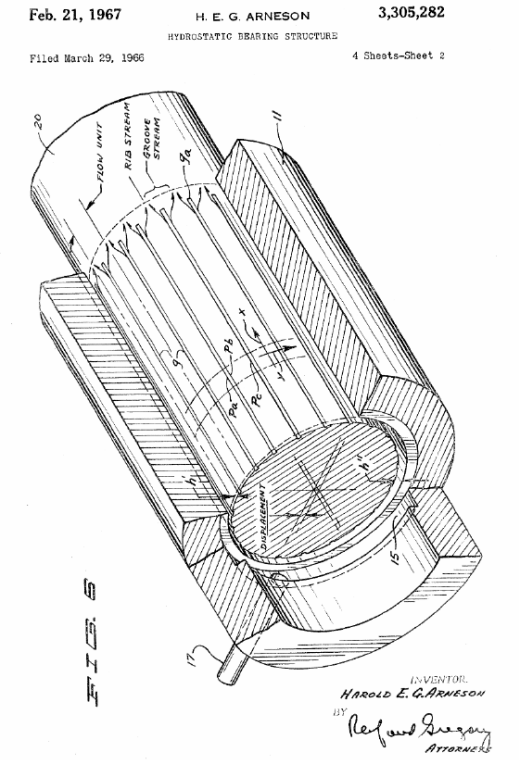

Figure 73. Hydrostatic bearing structure, patent number 3,305,282

Figure 73 is the original patent for the hydrostatic air bearing. In this bearing the air flows into the bearing from the outer stator and a cavity around the inner diameter of the bearing provides a constant pressure pocket. The air flows out of this pocket down along the lateral grooves, and out of the bearing. The lateral grooves provide regions of high and low pressure around the circumference of the bearing; therefore the bearing does not need to be hydrodynamic to carry a load. These pockets also present an increase in the load capacity and stiffness of the bearing.

Using these concepts a micro air bearing is designed, see Figure 74 and Figure 75. Assembly of the micro bearing is difficult, therefore the role of the stator and the rotor are reversed. Air is supplied through a hole in the center of the shaft and the air flows into a pocket

machined around the circumference of the shaft. A constant pressure pocket is created in the center of the bearing, and the air flows out of this pocket through the clearance gap. The ruby vee-jewel is pressed onto the end of the shaft, creating thrust-bearing regions on the top and bottom of the ruby orifice. The airflow through the gap suspends and constrains the rotor in all degrees of freedom, except rotational.

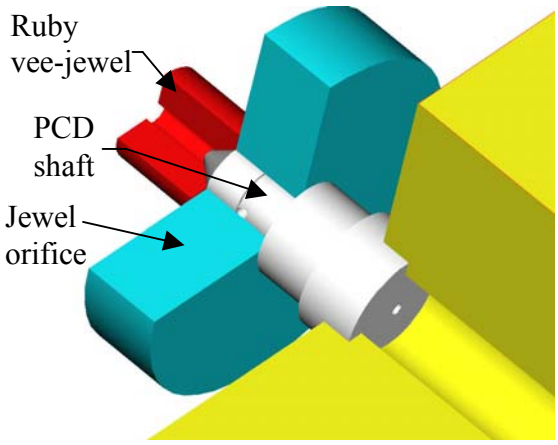

Figure 74. 3-d model of the micro air bearing

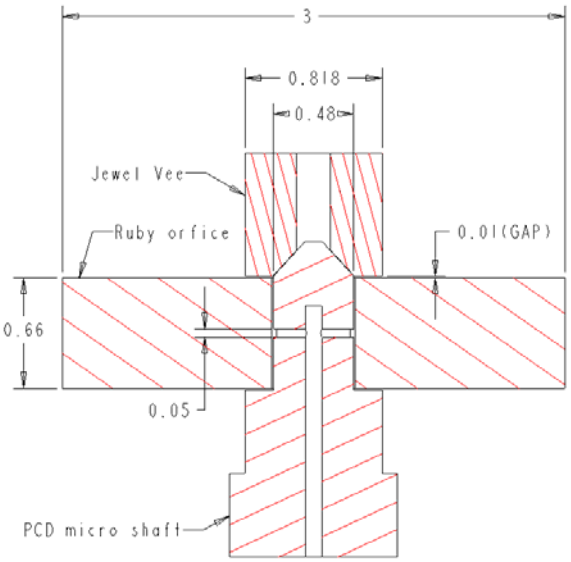

Figure 75. Cross section of micro air bearing, dimensions in mm.

Due to the complexity of achieving precise grooves on the micro scale, Polycrystalline Diamond (PCD) is chosen for the shaft material. The high surface roughness of the shaft will be used to achieve the regions of high and low pressure. A jewel orifice is selected for the rotor due

to the accuracy and low surface roughness of the hole. The through hole in the jewel will be trued with the PCD shaft before assembly.

6.2.2. Optical Fiber End Face machining

The use of optical fibers to transmit light waves was discussed in Chapter 5. Usually, the endface of the optical fiber is cleaved to a flat surface. When aligning optical fibers for sensing or connecting applications, perfect alignment of the endface of the optical fiber with the target surface is critical to performance. If the end-face of the optical fiber is machining to an optical shape, such as an asphere, then the shape of the beam can be controlled for more precise alignment with the target surface. Ductile mode grinding of the end-face can be achieved with a PCD tool like the one shown in Figure 76. The tool is rotated and plunged onto the optical fiber. A "lead in" will be machined into the tool so that precision alignment of the tool and optical fiber is not necessary.

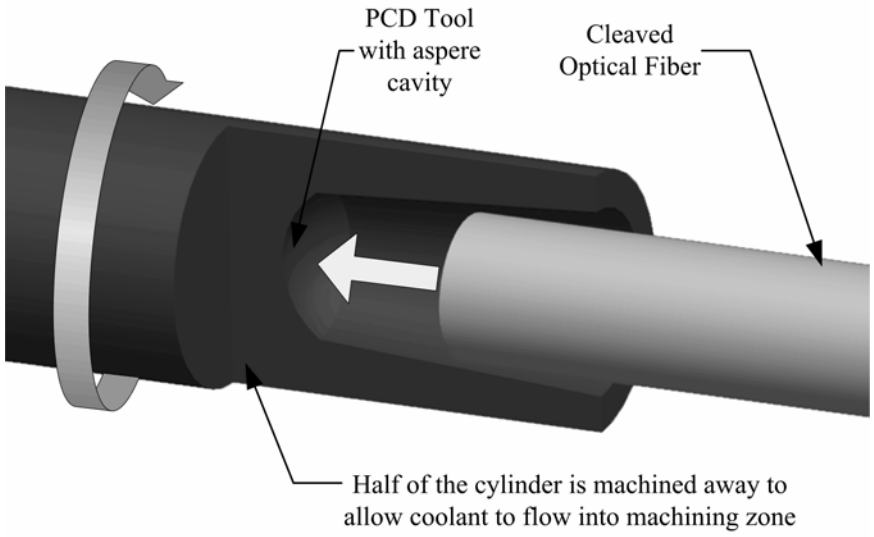

Figure 76. Optical fiber end-face machining, aspherical shape

Appendix A: Micro Shaft Straightness and Roughness

Table 7. The resulting straightness and roughness of 81 shafts fabricated with WEDG

Voltage (Volts)	Capacitance (pF)	Feed speed (μm/s)	Aspect Ratio	roughness Ra(μm)		straightness (μm)	
				Profile 1	Profile 2	Profile 1	Profile 2
70	10	1	10	0.1748	0.1531	4.2377	4.0079
			20	0.1568	0.1526	5.3078	5.0221
			30	0.1481	0.1388	4.8591	4.56
		3	10	0.3999	0.3412	6.6519	7.2177
			20	0.2013	0.2465	6.4208	5.921
			30	0.2199	0.2334	7.1137	5.9045
		5	10	0.1344	0.1356	3.6104	3.527
			20	0.1939	0.2089	4.7961	6.5179
			30	0.2242	0.2164	6.7853	6.9769
	220	1	10	0.1999	0.1892	4.0921	3.523
			20	0.3463	0.4576	6.5967	5.7001
			30	0.3037	0.5327	7.003	7.6373
		3	10	0.3824	0.3378	5.7563	5.9263
			20	0.2916	0.3071	6.7061	6.2788
			30	0.2941	0.2603	7.4918	6.5928
		5	10	0.6993	0.7811	7.1077	6.5116
			20	0.2858	0.2816	5.7138	5.3047
			30	0.2683	0.2413	7.0131	5.3558
	3300	1	10	0.3821	0.4051	5.1334	4.6077
			20	0.2355	0.2486	6.9655	5.1445
			30	0.2577	0.2822	6.0254	6.8375
		3	10	0.2413	0.2151	3.7884	3.0523
			20	0.2582	0.2427	5.3176	5.5215
			30	0.2766	0.211	5.3403	4.1285
		5	10	0.2347	0.2485	5.349	4.004
			20	0.2584	0.2644	5.1972	5.2006
			30	0.2073	0.2453	5.714	5.4048
100	10	1	10	0.1694	0.1782	3.8476	4.1864
			20	0.1487	0.1437	4.7906	4.8257
			30	0.2306	0.2103	7.7473	10.28
		3	10	0.1423	0.1343	4.2781	3.4154
			20	0.1907	0.1406	5.6396	5.8041
			30	0.1245	0.129	7.2959	6.0294
		5	10	0.3145	0.2919	5.1114	5.4888
			20	0.42	0.4181	5.7537	6.8467
			30	0.2523	0.2843	5.9438	7.6002
	220	1	10	0.2531	0.2164	4.7947	4.1849
			20	0.2864	0.2986	5.8589	5.5963
			30	0.1932	0.1772	5.2858	6.2133
		3	10	0.1935	0.1645	4.0329	3.6835

			20	0.1747	0.2324	6.2358	5.5866
			30	0.1875	0.206	4.5715	5.5714
		5	10	0.222	0.2143	7.4277	7.4238
			20	0.2478	0.2206	8.111	5.4779
			30	0.3328	0.3169	6.1761	6.4989
	3300	1	10	0.2995	0.3248	4.0944	5.6131
			20	0.2742	0.305	6.0061	6.1767
			30	0.2848	0.2443	5.9289	5.3502
		3	10	0.2668	0.3042	5.1348	5.3193
			20	0.2104	0.2623	4.8394	5.613
			30	0.2882	0.2006	5.8286	4.8395
		5	10	0.3264	0.3341	3.5749	4.3561
			20	0.295	0.2057	4.8313	4.6038
			30	0.126	0.2605	7.1478	6.7948
80	10	1	10	0.1714	0.1523	5.3491	4.7369
			20	0.1679	0.14	4.5863	4.7561
			30	0.1713	0.1589	5.1202	4.8418
		3	10	0.1492	0.0668	4.9789	3.9407
			20	0.1645	0.142	4.4952	5.3777
			30	0.1603	0.1582	4.886	5.7017
		5	10	0.1093	0.1029	4.9885	3.8964
			20	0.1322	0.1408	4.7607	4.6279
			30	0.1426	0.1466	4.2961	3.9221
	220	1	10	0.1894	0.1913	4.0054	4.2024
			20	0.1719	0.166	4.322	4.0757
			30	0.1819	0.1867	6.3569	5.8861
		3	10	0.2328	0.2202	4.0859	4.2144
			20	0.1906	0.1961	7.602	6.8067
			30	0.1717	0.1662	7.1885	7.1123
		5	10	0.2122	0.1825	4.4994	4.0965
			20	0.1712	0.2014	8.2621	7.737
			30	0.1823	0.1719	6.0879	5.6155
	3300	1	10	0.3339	0.3268	5.0609	5.4461
			20	0.2324	0.2459	5.713	5.1512
			30	0.2549	0.2305	9.1017	5.9381
		3	10	0.2629	0.2705	5.0597	5.2486
			20	0.2748	0.305	5.6475	6.125
			30	0.3227	0.2498	10.2227	6.949
		5	10	0.2504	0.2924	4.8802	6.0451
			20	0.2366	0.2266	5.5381	5.5942
			30	0.2591	0.2498	12.0409	6.949

Appendix B: Discharge Current Measurements

9/18/01
Discharge waveform of 114 diameter electrode, capacitor #1, 110 Volts.
Wave occupies 200 nanoseconds and Vp-p is approximately 5 Volts. The sensitivity of the prove is 5mv/mA, therefore the Ap-p is approximately 1 Ampere.

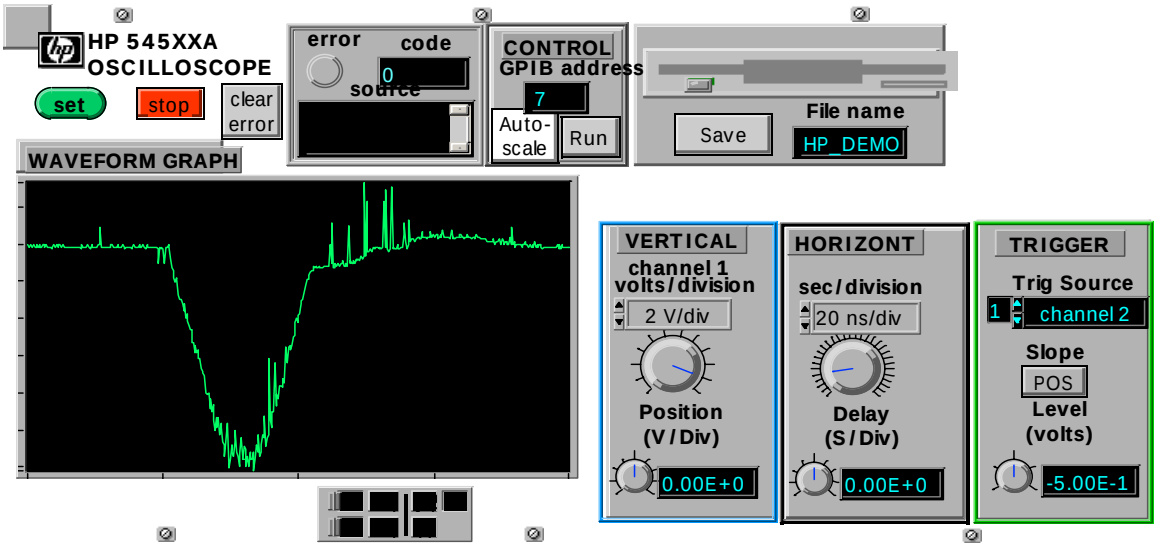

Appendix C: Discharge Force measurements

Analysis of electro-discharge forces

$\phi_w := -110V$ $e := 1.6 \cdot 10^{-19} C$ $m_{carbon} := 12\ amu$ $m_i := 1.67 \cdot 10^{-24} \cdot \frac{m_{carbon}}{1000} kg$ $I := 1A$

$$P := 2 \cdot I \cdot \sqrt{\frac{-2 \cdot m_i \cdot \phi_w}{e}}$$

$\sigma_{ult} := 1400 \cdot 10^6 Pa$ $E := 411 \cdot 10^9 Pa$

$$ar_{max\_discharge}(d) := \frac{\pi \cdot \sigma_{ult} \cdot d^2}{32 \cdot P}$$

$$\delta_{max\_discharge}(d) := \frac{64 \cdot P \cdot ar_{max\_discharge}(d)^3}{3\pi \cdot E \cdot d}$$

$$ar_{experimental} := \begin{pmatrix} 10 \\ 33.333 \\ 40 \\ 50 \\ 71.43 \end{pmatrix} \quad d_{exp} := \begin{pmatrix} 5 \cdot 10^{-6} \\ 30 \cdot 10^{-6} \\ 50 \cdot 10^{-6} \\ 100 \cdot 10^{-6} \\ 140 \cdot 10^{-6} \end{pmatrix}$$

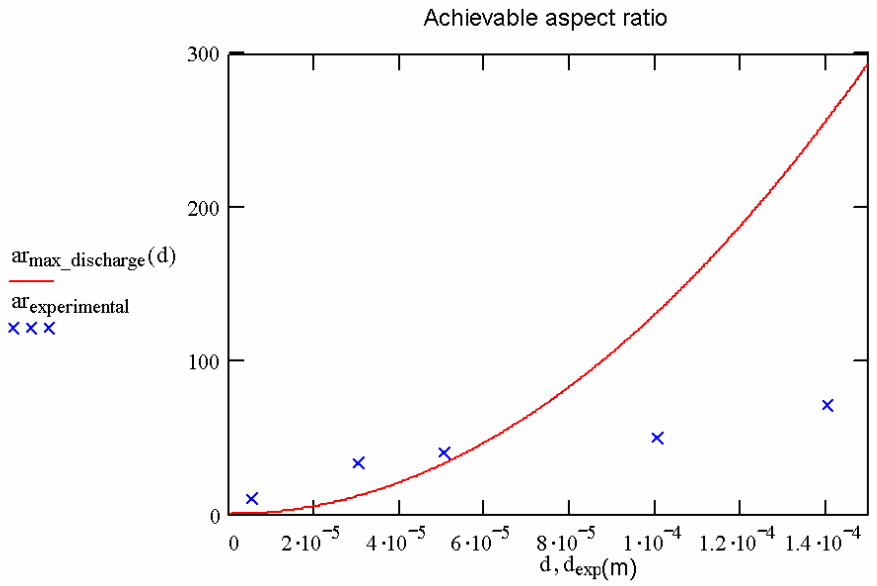

References

[1] Kurafuji, H. and Masuzawa, T. “Micro-EDM of cemented carbide alloys”. *Japan Society of Electrical-Machining Engineers* (2) 3, 1-16, 1968.

[2] Allen, David M. “Microelectrodischarge Machining”. Chapter 7 of book entitled “Micro Machining of Engineered Materials”. Marcel Dekker, Inc. 2002.

[3] Masuzawa, T. “Wire Electro-Discharge Grinding for Micro-Machining”. *Annals of the CIRP*. Vol. 34, No. 1. 1985. p. 431-434.

[4] Sato, T., T. Mizutani, and K. Kawata. "Electro-Discharge Machine for Micro Hole Boring". *National Technical Report*. Vol. 81, No. 5. Oct. 1985. p. 105-113.

[5] Masuzawa, T., C.-L. Kuo, and M. Fujino. “A Combined Electrical Machining Process for Micronozzle Fabrication”. *Annals of the CIRP*. V. 43, N. 1. 1994, p 189-192

[6] Allen, D.M. and A. Lecheheb. "Micro Electro-Discharge Machining of Ink Jet Nozzles: Optimum Selection of Material and Machining Parameters". *Journal of Materials Processing Technology*. Vol. 58. 1996. p. 53-66.

[7] Masuzawa, T., Y. Hamasaki, and M. Fujino. “Vibroscanning Method of Nondestructive Measurement of Small Holes”. *Annals of the CIRP*. V. 42, N. 1. 1993. p. 589-592.

[8] Masuzawa, T., B.J. Kim, C. Bergaud, and M. Fujino. “Twin-probe Vibroscanning Method for Dimensional Measurement of Microholes”. *Annals of the CIRP*. V. 46, N. 1. 1997. p. 437-440.

[9] Yu, Z., T. Masuzawa, and M. Fujino. "Micro-EDM for Three Dimensional Cavities - Development of Uniform Wear Method". *Annals of the CIRP*. Vol. 47, No. 1. p. 169-172.

[10] Yu, Z., T. Masuzawa and M. Fujino. "3D Micro EDM with Simple Shape Electrode: Part 1 -- Machining of Cavities with Sharp Corners and Electrode Wear Compensation". *International Journal of Electrical Machining*. No. 3. p. 7-12. 1998.

[11] Yu, Z., K.P. Rajurkar, and P.D. Prabhuram. “Study of Contouring Micro EDM Characteristics”. *Proc. of the 10th Int. Conf. on Precision Engineering*. Japan Society for Precision Engineering (JSPE). Yokohama, Japan. July 18-20, 2001. Kluwer Academic Publishers, Boston, MA. P. 199-203.

[12] Toshihiko, WADA, Takeshi MASAKI and David W. Davis. “Development of Micro Grinding Process using Micro EDM trued Diamond Tools”. *ASPE Proceedings, Annual Conference, 2002*. p. 16-19.

[13] Thoe, T.B., D.K. Aspinwall, M.L.H. Wise, I.A. Oxley. “Polycrystalline Diamond Edge Quality and Surface Integrity Following Electrical Discharge Grinding”. *Journal of Materials Processing Technology.* V. 56, 1996. p. 773-785.

[14] Liu, Y.H., Y.F. Guo, and J.C. Liu. “Electric Discharge Milling of Polycrystalline Diamond”. *Institution of Mechanical Engineers.* V. 211 Part B, 1997. p. 643-647.

[15] Zhong, Zhaowei. “Surface Finish of Precision Machined Advanced Materials”. *Journal of Mechanical and Production Engineering.* V. 122, 2002. p. 173-178.

[16] Cheng, Kai “Abrasive Micromachining and Microgrinding”. Chapter 4 of book entitled “Micro Machining of Engineered Materials”. Marcel Dekker, Inc. 2002.

[17] Bifano, Thomas G., and Steven C. Fawcett. “Specific Grinding Energy as an In-Process Control Variable for Ductile-Regime Grinding”. *Precision Engineering.* V. 13, N. 4. October 1991. p. 256-262.

[18] Ngoi, B.K.A., and P.S. Sreejith. “Ductile Regime Finish Machining – A Review”. *The International Journal for Advanced Manufacturing Technology.* V. 16, 2000, p. 547-550.

[19] Bifano, T.G., T.A. Dow, and R.O. Scattergood. “Ductile-Regime Grinding: A New Technology for Machining Brittle Materials”. *Journal of Engineering for Industry.* V. 113, May 1991, p. 184-189.

[20] Golini, D., and S.D. Jacobs. “Physics of Loose Abrasive Microgrinding”. *Applied Optics*. V. 30, 1991. p. 2761-2777.

[21] Subramanian, K., S. Ramanath, M. Tricard. “Mechanisms of Material Removal in the Precision Production Grinding of Ceramics”. *Journal of Manufacturing Science and Engineering.* V. 119. 1997. p. 509-518.

[22] Egashira, K. and K. Mizutani. “Micro-Drilling of Monocrystalline Silicon Using a Cutting Tool”. *Precision Engineering*. V. 26, N. 3. July, 2002. p. 263-268.

[23] Masaki, T., T. Mizutani, K. Yonemaochi, and A. Tanaka. "Electric Discharge Machining Method and Apparatus for Machining a Microshaft". United States Patent and Trademark Office. Patent Number 4,900,890. Feb. 13, 1990.

[24] Raja, J., B. Muralikrishnan, S. Fu. "Recent Advances in Separation of Roughness, Waviness, and Form". *Precision Engineering*. V. 26, N. 2. 2002. p. 222-235.

[25] Weber, T., S. Motavalli, B. Fallahi, and S.H. Cheraghi. "A Unified Approach to Form Error Evaluation". *Precision Engineering*. V. 26, N. 3. July 2002. p. 269-278.

[26] Serrano, Sergio. *Engineering Uncertainty and Risk Analysis*. Hydro Science Inc., 2001.

[27] Estler, Tyler. "Calibration and Use of Optical Straightedges in the Metrology of Precision Machines". *Optical Engineering*. V. 24, N. 3. 1985, p. 372-379.

[28] Singh, Ajit, and Amitabha Ghosh. "A thermo-electric model of material removal during electric discharge machining". *International Journal of Machine Tools & Manufacture*. V. 39, 1999, p. 669-682.

[29] Clauser, F.H. "Syposium of Plasma Physics". Addison-Wesley Publishing company, Inc., 1960.

[30] Panasonic. "Operating Instructions". Manual provided with Panasonic MG-ED72W micro-EDM machine. Document No. FA-YN8201, T069AE, Q512002E.

[31] Masaki, Takeshi. Conversations at the Panasonic Production Engineering Facility. July 2002.

[32] Ravi, N. and H. Huang. "Fabrication of Symmetrical Section Microfeatures Using ElectroDischarge Machining Block Electrode Method". *Journal of Micromechanics and Microengineering*. V. 12. 2002. p. 905-910.

[33] Ravi, N. and S.X. Chuan. "The Effects of ElectroDischarge Machining Block Electrode Method for Microelectrode Machining". *Journal of Micromechanics and Microengineering*. V. 12. 2002. p. 532-540.

Vita

Christopher James Morgan was born in Danville, Kentucky, on July 12, 1979, the son of Sherri Lee Morgan and John Neil Morgan. After completing his work at Boyle County High School, Boyle County, Kentucky, in 1997, he entered the University of Kentucky Lexington, Kentucky. While attending the University of Kentucky he participated in a Cooperative Education program and was employed by Mathews Conveyor in Danville, Kentucky. He received the degree of Bachelor of Science with a major in Mechanical Engineering from the University of Kentucky in May 2002. In June 2002, he entered the Graduate School of The University of Kentucky.

Honors:
Tau Beta Pi Engineering Honor Society, Phi Eta Sigma Honor Society, Golden Key Honor Society, Recipient of TVA University Scholar Fellowship, Recipient of Paul Orberson Academic / Athletic Scholarship, Awarded to Dean's list, 7 semesters.

Publications:

Vallance, R.R., C. Morgan, and A.H. Slocum. "Precisely Positioning Pallets in Multi-Station Assembly Systems". *Journal of the International Societies for Precision Engineering and Nanotechnology*. Vol. 28. pp. 218-231. April 2004.

Vallance, R.R., C. Morgan, S. Shreve and Eric Marsh. "Micro Tool Characterization using Scanning White Light Interferometry". Accepted for publication in *Journal for Micromechanics and Microengineering*.

Morgan, C., Eric Marsh and R.R. Vallance. "Micro Machining Glass with Polycrystalline Diamond Tools Shaped by Micro Electro-discharge Machining". *Journal for Micromechanics and Microengineering*. Vol. 14 (2004) 1687-1692.

Morgan, C., S. Shreve, and R.R. Vallance. "Precision of Micro Shafts Machined with Wire Electro-Discharge Grinding". Proceedings of the Winter Topical Meeting on Machines and Processes for Micro-Scale and Meso-Scale Fabrication, Metrology, and Assembly. American Society for Precision Engineering (ASPE). University of Florida. Gainesville, FL. January 22-23, 2003.